Dosage sensitivity in Pumilio1-associated diseases involves two distinct mechanisms

Salvatore Botta[1,2], Nicola de Prisco[1], Alexei Chemiakine[1], Maximilian Cabaj[1], Purvi Patel[3], Rajesh K. Soni[3], and Vincenzo A. Gennarino[1,4,5,6,7]

[1]Department of Genetics and Development, Columbia University Irving Medical Center, New York, NY.
[2]Department of Translational Medical Science, University of Campania Luigi Vanvitelli, Caserta, Italy.
[3]Proteomics and Macromolecular Crystallography Shared Resource, Herbert Irving Comprehensive Cancer Center, Columbia University Irving Medical Center, New York, NY.
[4]Departments of Pediatrics and Neurology, Columbia University Irving Medical Center, New York, NY.
[5]Columbia Stem Cell Initiative, Columbia University Irving Medical Center, New York, NY.
[6]Initiative for Columbia Ataxia and Tremor, Columbia University Irving Medical Center, New York, NY.
[7]Corresponding author: Vincenzo A. Gennarino, Department of Genetics and Development, Columbia University Irving Medical Center, 701 West 168th Street, HHSC 1402 New York, NY 10032; +1 212-305-7863; vag2138@cumc.columbia.edu

Abstract

Mutations in the RNA-binding protein (RBP) Pumilio1 (PUM1) can cause dramatically different phenotypes. Mild mutations that reduce PUM1 levels by 25% lead to a mild, adult-onset ataxia, whereas more severe mutations that reduce PUM1 levels 40-60% produce an infantile syndrome involving multiple developmental delays and seizures. Why this difference in expression should cause such different phenotypes has been unclear; known PUM1 targets are de-repressed to equal degrees in both diseases. We therefore sought to identify PUM1's protein partners in the murine brain. We identified a number of putative interactors involved in different aspects of RNA metabolism such as silencing, alternative splicing, and polyadenylation. We find that PUM1 haploinsufficiency alters the stability of several interactors and disrupts the regulation of targets of those interactors, whereas mild PUM1 loss only de-represses PUM1-specific targets. We validated these phenomena in patient-derived cell lines and show that normalizing PUM1 levels rescues the levels of interactors and their targets. We therefore propose that dosage sensitivity does not necessarily reflect a linear change in levels but can involve distinct mechanisms. Studying the interactors of RBPs *in vivo* will be necessary to understand their functions in neurological diseases.

Introduction

To quickly respond to a specific perturbation, cells must modify their protein repertoire. RNA-binding proteins (RBPs) accomplish this at the post-transcriptional level, regulating RNA localization, transport, translation, splicing, and decay; they have been found to orchestrate hundreds of pathways that are responsible for proper biological functions (1, 2). RBPs can coordinate or compete with each other or exert mutual influence (3), and they also interact with microRNAs (miRNAs) to suppress the expression of their target genes by binding to a short complementary seed region in the 3' UTRs of mRNAs. RBPs and microRNA machinery are particularly important in neurons, whose plasticity demands a rapid local response to stimuli that can be quite distant from the nucleus (4). It is therefore not surprising that disruptions in RBPs underlie several complex neurological disorders. For example, large CAG expansions in the RBP FMRP cause Fragile X syndrome, but milder "premutations" in FMRP cause adult-onset Fragile X-associated tremor and ataxia syndrome (FXTAS) (5). The RBPs TDP43 and FUS are both involved in amyotrophic lateral sclerosis, and TDP43 mutations is linked to frontotemporal dementia (6, 7). Despite increasing interest in how RBPs influence neuronal function through target regulation, we still know relatively little about RBP interactions and regulation (7-9).

Our recent work on the RBP Pumilio1 (PUM1) has led us to consider RBP interactions. We found that mutations in PUM1 that reduce its levels by 40-60% cause a neurodevelopmental disease in humans (PUM1-associated developmental delay and seizures, or PADDAS). PADDAS causes cognitive, speech, and motor delays and seizures. On the other hand, mild mutations in PUM1 that reduce its levels by only 25% lead to a slowly progressive, pure ataxia with onset in mid-life (PUM1-related cerebellar ataxia or PRCA). Although the severity of the PRCA and PADDAS phenotypes tracks with the levels of functional PUM1, precisely what is happening at the molecular level remains unclear. PUM1 contains a highly conserved RNA-binding domain composed of eight tandem repeats known as Puf homology domains (HDs). While the mutation that produces mild disease (PRCA), T1035S, lies within the HD domain and impairs RNA binding, the most severe PADDAS mutation (R1147W) lies outside this domain and does not impair RNA binding (10, 11). Moreover, known PUM1 targets are upregulated to similar degrees in the PRCA and PADDAS patient cell lines (10). This suggested to us that PRCA might be caused by deregulation of PUM1 targets, whereas PADDAS might result from disruption of PUM1's interactions with its protein partners along with de-repression of the targets of these complexes.

Testing this hypothesis requires identifying PUM1 interactors in the mouse brain. Although a great deal is known about the PUMILIO/FBF (PUF) family of RBPs (12-20), of which PUM1 and its homolog PUM2 are members, little is known about PUM1 function in the postnatal mammalian brain. Protein interactions in general, and those of PUF family members specifically, can be organism-, transcript-, and

even condition-specific (21). We therefore took an unbiased approach by using *in vivo* proteomics to identify PUM1's native partners. Since *Drosophila* studies show that Pumilio can change its protein partners in different neuronal types (22), we first examined the brain as a whole and then repeated our analyses in three distinct brain regions that most highly express PUM1. We then determined the effect of loss of PUM1 on a subset of RBP interactors that were the most highly connected within the interactome, using *PUM1* heterozygous and homozygous null mice and patient-derived cell lines. We identified targets shared among these interactors and examined their responses to PUM1 insufficiency in mice and cell lines from patients bearing the T1035S and R1147W mutations. These data underscore the need to examine all the interactions an RBP is engaged in.

Results

Establishing the Pumilio1 interactome across the adult mouse brain

To identify interactors of Pum1 (the murine protein), we performed co-immunoprecipitation (IP) for Pum1 on whole brains from 10-week-old wild-type (WT) mice, followed by liquid chromatography with tandem mass spectrometry (LC-MS/MS, or simply mass spec); we used IP against IgG (IP-IgG) as a negative control (see Methods). Post-IP western blot detected no residual Pum1 from brain tissue confirming that our protocol recovers virtually all of Pum1 (Supplemental Figure 1). To increase the likelihood that our candidates would prove to be genuine interactors, we required putative interactors to have at least two unique peptides present in at least five out of six IP-Pum1 samples compared to IP-IgG in label-free quantification intensity (LFQ-intensity, see Methods).

This analysis yielded 412 putative Pum1 interactors (Supplemental Figure 2A and Supplemental Table 1). We incorporated mammalian protein-protein interaction data from CORUM and the Human Protein Atlas by using g:GOSt (g:Profiler; see Supplemental Methods) (23) to reveal 22 clusters of functionally related proteins (Supplemental Figure 2A). Among the putative interactors we found those that have been previously identified, supporting the validity of our approach. For example, our mass spec identified Pum2 and Fmrp, which associate with Pum1 in neural progenitor cells (24). Other identified proteins belong to families previously found to interact with PUM1 *in vitro*, such as CNOT1, which is the central scaffold of the CCR4-NOT complex (16, 25), which PUM1 recruits to shorten poly(A) tails and promote mRNA degradation (15-17). Translation initiation factors (cluster 3) have been found to cooperate with Puf proteins in other species (26), and human PUM2-mediated repression was found to require PABPC1, while our mass spec yielded Pabpc4 (17). Cluster 8, which includes proteins that have been associated with RNA fate regulation, was the most strongly interconnected with other clusters.

Given the plethora of putative interactors, and the tissue-specificity of interactions (22), we repeated

the mass spec experiments on the cerebellum, hippocampus, and cortex, where Pum1 is most highly expressed (11). Scatter-plots and PCA showed a clear separation of Pum1 and IgG samples (Supplemental Figure 3A-D). Through this analysis we identified 854 putative Pum1 interactors in the cerebellum, 423 in the hippocampus, and 598 in the cortex (Figure 1A; Supplemental Table 1). 467 were unique to the cerebellum, 140 to the hippocampus, 229 to the cortex, and 154 unique to the rest of the brain (i.e., excluding these three regions). Only 88 candidates were shared among these three brain regions and the whole brain (Figure 1A*, yellow dots*). Interestingly, the only brain region to show interaction between Pum1 and Pum2 was the cortex (Supplemental Figure 4A), despite the fact that Pum2 is expressed at roughly the same levels in the three brain regions (Supplemental Figure 4B).

This region-specific analysis yielded the same components of the APC/C (Supplemental Figure 4C) and mTOR pathways (Supplemental Figure 4D) across the three brain regions, but expanded the list of Pum1 interactors in several other afore-mentioned pathways (Figure 1A, Supplemental Figure 4C-E). For example, Cnot1 and Cnot2 turned up in all three brain regions, while Cnot10 appears to be cortex-specific (Figure 1A, Supplemental Figure 4E). There were many proteins involved in translation initiation, with Eif3b being specific to the hippocampus (Supplemental Figure 4E). Rbfox1 was specific to the cortex, and Rbfox2 to the cerebellum and hippocampus (Figure 1A), consistent with previous work showing that Rbfox1 mediates cell-type-specific splicing in cortical interneurons (27) and that Rbfox2 is needed for cerebellar development (28).

We then performed DAVID Gene Ontology analysis for hits from both the whole brain and from each brain region analyzed (Figure 1B and Supplementary Table 2). The main categories identified were ubiquitin ligases (anaphase-promoting complex [APC/C], E2/E3 and Kll-linked ubiquitin) and RBPs involved in various aspects of RNA metabolism (RNA silencing, 3'UTR binding, mRNA stability, transport, and splicing). We prioritized the RBPs in cluster 8 (Supplemental Figure 2)—Fmrp and Ago2 (involved in RNA silencing), Pum2, Cnot1, and Rbfox3 (an alternative splicing factor)—for the following reasons. First, this cluster was the most highly interconnected with other clusters; second, RNA-related categories were prominent in the gene ontology analyses for both whole brain and all three brain regions; third, these RBPs have been well studied and would allow us to more readily test the consequences of PUM1 loss; fourth, these proteins are associated with Pum1 in whole brain; lastly, these proteins have been studied mostly *in vitro* and have never been associated with Pum1 in the murine brain.

Pum1 associates with Pum2, Fmrp, Ago2, and Cnot1 in the absence of mRNA

The associations of Pum1 with Pum2, Fmrp, Ago2, Rbfox3, and Cnot1 were confirmed by co-IP followed by western blot (Figure 2A, *left panel*). Since Fmrp and Ago2 both bind Mov10 *in vitro* (29,

30), we also blotted for murine Mov10. Mov10 was pulled down with Pum1, likely in concert with Fmrp (Figure 2A). We co-IPed Pum1 and blotted for all six RBPs in *Pum1*$^{-/-}$ mouse brains and detected none of them (Supplemental Figure 5A), indicating that the Pum1 antibody we used is specific. As negative controls, we tested other proteins associated with the RISC complex (Ago1 and Ago3) that did not appear in our mass spec data, and our co-IP experiments found no interactions (Supplemental Figure 5B).

To exclude the possibility that the co-IPs recovered proteins that are co-bound to target RNAs but are not part of the same complex as the protein of interest, we treated mouse brain samples with RNase and verified that no detectable RNA remained (see Methods). Pum1 still associated with Pum2, Fmrp, Ago2, and Cnot1 in the absence of mRNA, but not with Rbfox3 or Mov10 (Figure 2A, *right panel*). We repeated the RNase experiments in HEK293T cells, which confirmed our results (except for RBFOX3, which was not detectable in these cells) (Figure 2B). These data suggest that Pum1 interacts with all the six RBPs in brain, and this interaction is RNA-independent.

Some interactions among these RBPs require PUM1

To confirm the interaction between Pum1 and the six RBPs and to understand the reciprocal interactions among the interactors themselves, we performed reciprocal co-IP in wild-type and *Pum1*$^{-/-}$ 10-week-old mouse brains for Pum2, Ago2, Fmrp, Cnot1, Rbfox3, and Mov10. We first confirmed that IP against each of these six RBP is pulling down Pum1 from WT but not from *Pum1*$^{-/-}$ mouse brain (Figure 3A-F). Pum2 interacted with Cnot1 only in the presence of Pum1 (Figure 3A). Unexpectedly, Fmrp associated with Mov10 and Rbfox3 only in the presence of Pum1 (Figure 3B-D). Fmrp and Cnot1 did not associate in WT brain (Figure 3B, *left*) but did so in the absence of Pum1 (Figure 3B, *right*). Ago2 associated with Pum1, Fmrp, Cnot1 and Mov10 in WT brain, but in the absence of Pum1 it no longer interacted with Fmrp or Mov10 (Figure 3E). Mov10 associated with Fmrp but not with Ago2 (Figure 3D and E). Rbfox3 associated with Cnot1 (Figure 3C) but not *vice versa* (Figure 3F). IPs against Pum2, Ago2, Fmrp, Cnot1, Rbfox3, and Mov10, performed in the presence or absence of RNA in WT and *Pum1*$^{-/-}$ mouse brains (Supplemental Figure 6A-F) confirmed that, in the absence of Pum1, these interactions require RNA.

In summary, Pum1 associates with Pum2, Fmrp, Ago2, and Cnot1, with or without RNA (Figure 3A-F and Supplemental Figure 6A-F). Pum1 seems to be required for association between Fmrp, Mov10 and Rbfox3, and between Ago2 and Fmrp, Mov10, and Cnot1. In the absence of Pum1, the associations between Pum2, Fmrp, Ago2 and Cnot1 require RNA (Supplemental Figure 6A-F). These data suggest that the interaction between Pum1 and these RBPs seems to be prior binding the RNA.

Pum1 loss alters levels of RBP interactors in mouse cerebella by brain region and sex

If Pum1 is an important interactor for these six RBPs, loss of Pum1 should affect their stability or abundance. *Pum1* heterozygous and homozygous null mice showed changes in the quantities of Pum2, Ago2, and Mov10 proteins across the brain (Supplemental Figure 7A), but only *Pum2* showed changes in mRNA levels (Supplemental Figure 7B). Since Ago2 and Mov10 levels fell only in male mice (Supplemental Figure 7A), we quantified Pum2, Fmrp, Ago2, Rbfox3, Cnot1 and Mov10 in the cerebellum, cortex, and hippocampus of male and female mice. We first measured Pum1 mRNA and protein levels to confirm the reduction of Pum1 in our $Pum1^{+/-}$ or $Pum1^{-/-}$ mice in each brain region (Figure 4A-C, and Supplemental Figure 8). Pum2 protein levels rose in all three brain regions, as did its mRNA (Figure 4A-C, and Supplemental Figure 8).

As previously reported, Fmrp protein expression was upregulated in all three brain regions in male KO mice, but in female KO cerebella Fmrp was reduced by almost 70% (Figure 4A) (31, 32). Three other proteins also showed divergent responses to Pum1 loss according to sex and brain region: Ago2, Rbfox3 (in the hippocampus), and Cnot1 (in the cerebellum) (Figure 4A-C). None of these proteins showed any changes in mRNA levels (Supplemental Figure 8), despite the fact that *Fmr1* and *Cnot1*, like *Pum2*, have a Pumilio Response Element (PRE) (33) in their 3'UTR. In summary, these data suggest that loss of Pum1 could cause a sex- and region-specific reorganization of these complexes, or that there are additional sex-specific Pum1 interactors.

Pum1 loss dysregulates Ago2 and the microRNA machinery in mouse cerebella by sex

To confirm these Pum1 sex-specific functions—and because Pum1 loss has deleterious effects on the cerebellum in both mice (11) and humans (10)—we asked whether the divergence of Ago2 protein levels in males and females extended to cerebellar miRNAs. A miRNAseq found 701 expressed miRNAs, many of which diverged in expression between the two sexes (Supplemental Figure 9). Hierarchical heatmap clustering of significant miRNA expression in $Pum1^{-/-}$ and WT male and female cerebella at 10 weeks of age revealed that the expression of 166 miRNAs (Supplemental Table 3) diverged between the two sexes in parallel with Ago2 expression (Figure 4D).

To examine the functional consequences of this Ago2/miRNA dysregulation, we studied the expression of downstream targets that are co-bound by those miRNAs in 10-week-old WT and $Pum1^{-/-}$ male and female cerebella. To perform this experiment we selected all the miRNAs with at least a 25% change in expression in either direction, for a total of 49 miRNAs. Using TargetScan and CoMeTa (34, 35) we identified 6832 putative targets that are co-bound by at least 2 out of 49 possible miRNAs. We prioritized targets that are co-bound by at least 8 miRNAs, for a total of 49 putative targets. $Pum1^{-/-}$ male and female cerebella showed gene expression changes for 44 out of these 49 targets, which correlated

198 with the sex-dependent differences in Ago2 levels (Figure 4E, Supplemental Figure 10 and Supplemental
199 Table 4).
200 To elucidate the biological pathways in which these miRNAs play an essential role, we performed
201 David Gene Ontology with all the non-redundant targets predicted by CoMeTa (35) and TargetScan 7.1
202 (34) that are co-bound by at least four miRNAs. This analysis yielded 2127 targets (Supplemental Figure
203 11A-C). Under "cellular components" there was an enrichment in multiple categories having to do with
204 synaptic function. Under "biological processes" the most enriched categories are organ growth and post-
205 embryonic development (PADDAS children have growth defects (10), consistent with this GO analysis).
206 Under KEGG pathways, there was a particular enrichment in Wnt signaling, dopaminergic and
207 cholinergic pathways, cancers (increased Pum1 levels have been described in several cancers (36-38)),
208 protein ubiquitination (which accords with interactions with the APC/C complex).
209 To understand the neuron-related biological pathways, the same targets were analyzed by SynGO
210 (39), a curated ontology analysis based on genes that are exclusively expressed in specific neurons from
211 single-cell data. SynGO confirmed that 117 targets are presynaptic, whereas 124 are postsynaptic
212 (Supplemental Figure 11D). Moreover, among the 166 miRNAs inversely expressed between sexes, we
213 found the entire miR-200 family (miR-200a, miR-220b, miR-200c, miR-141, and miR-429), which has
214 been reported to regulate crucial targets involved in neurogenesis, glioma, and neurodegenerative diseases
215 (40, 41). Overall, these results are consonant with our mass spec and suggest an intimate relation between
216 Pum1 and Ago2 in mouse cerebellum.
217
218 *Pum1, Pum2, Fmrp, Ago2, and Rbfox3 share their top targets*
219 If indeed the complexes Pum1 forms with these RBPs are physiologically relevant, as seen for Ago2
220 in cerebellum, then they should co-regulate at least some of the same mRNA targets. Indeed, one
221 corollary of the "regulon theory," which posits that mRNA targets in the same pathway are co-regulated
222 (2, 42-44), is that there should be a discernible set of RBPs that do the co-regulating.
223 To test this hypothesis, we analyzed all the high-throughput sequencing UV-crosslinking and
224 immunoprecipitation (HITS-CLIP) data available from the murine brain (such data exist for Fmrp (45),
225 Ago2 (46), Rbfox3 (47), Pum1, and Pum2 (24)). We then performed gene set enrichment analysis
226 (GSEA) (48) using Fmrp as the basis for comparison (because it has the largest dataset). As negative
227 controls, we used HITS-CLIP data from mouse brain for four RBPs that did not show up as Pum1
228 interactors in our mass spec: Mbnl2 (49), Nova (50), Apc (51), and Ptpb2 (52).
229 This analysis revealed that Pum1 targets were preferentially distributed in the top 5th percentile of all
230 Fmrp targets, with an enrichment score (ES) of 0.93 (the maximum is 1) and a FDR of 0 (Figure 5A**,** *blue*

line represents ES). Pum2, Ago2, and Rbfox3 showed nearly identical patterns (Figure 5A). There was no significant overlap between the targets of Fmrp and those of any negative control (Nova had the highest ES, but this was only 0.36 with a rank max of 45th percentile and FDR=1; Figure 5B). Neither Pum1, Pum2, Rbfox3, Fmrp, nor Ago2 targets were enriched among any of the ranked target lists of the negative controls (Supplemental Figure 12A**,** and *data not shown*).

To ascertain that the highest-ranking Fmrp targets correspond to the genes with the highest probability of being Pum1 targets, we divided the Fmrp ranked target list into 10 equal bins according to percentile. We then repeated GSEA of Pum1 HITS-CLIP data for each bin and found that 648 of the 1194 identified Pum1 targets (54%) are in the top 10th percentile of Fmrp targets, with an ES of 0.8 (Figure 5C). This was also true for Pum2, Ago2, and Rbfox3 (Figure 5C).

We performed the same analysis using the Pum1 target list as the basis for comparison. We ran GSEA on each of the four Pum1 partners against the list of Pum1 target genes, and each partner's targets are within the top 20% of the Pum1 list (Figure 5D). Specifically, Fmrp's targets reside in the top 10th percentile (with an ES of 0.81), Pum2's targets within the 16th percentile (ES=0.9), Ago2's targets within the 18th percentile (ES=0.76), and Rbofx3's targets within the 19th percentile (ES=0.67). The four RBPs used here as negative controls have a minimum rank at the 37th percentile, and the best ES was 0.26 for Apc; none of the five reached statistical significance (Figure 5D). These analyses demonstrate that there is substantial overlap among the highest-ranked targets of Pum1, Pum2, Fmrp, Ago2, and Rbfox3.

We also studied the targets shared by Pum1, Pum2, Ago2, and Rbfox3 to determine how they distribute within Fmrp. We found an ES of 0.93 falling within the top 5th percentile (Figure 5E); 141 out of 175 common targets were within the top 10th percentile (bin 1) of Fmrp targets, with 99 within the top 5th (Figure 5F). This contrasts with the negative controls, for which the best ES was 0.41 within the top 40th-60th percentile (Figure 5G). DAVID gene ontology analysis of those 175 common targets between Ago2, Pum1, Pum2, Fmrp, and Rbfox3 revealed pathways enriched in neurons and axonal projections (Supplemental Figure 12B and C). Previous studies have shown that Pum1 and Pum2 cooperate with the miRNA machinery to suppress certain targets (11, 13). Among Fmrp HITS-CLIP targets, there were almost 300 microRNAs. Pum1 HITS-CLIP has 60 miRNAs, only four of which are not shared with Fmrp; Pum2 HITS-CLIP has no miRNAs that are not shared with either Pum1 or Fmrp (Supplemental Figure 12D and Supplemental Table 6).

PUM1 interactors are destabilized in cell lines from PADDAS, but not PRCA, patients

Having identified Pum1 interactors and shared targets, we asked whether mutations associated with either mild or severe disease destabilize human PUM1 interactors in patient-derived cell lines. For

PADDAS, we compared fibroblasts from one 9-year-old female patient (R1147W) with fibroblasts from three different 9-year-old female healthy controls. For PRCA, we compared lymphoblastoid cells from two female PRCA patients (both with the T1035S mutation; 59 and 58 years old, respectively) with lymphoblastoid cells from three different 58-year-old female healthy controls (10). IP against PUM1 followed by western blot showed that PADDAS cells had 49%, and PRCA cells 76%, of the amount of PUM1 found in healthy controls (Supplemental Figure 13A and B), consistent with our previous report (10). Post-IP did not detect any residual PUM1 from PADDAS or PRCA cell lines, or their controls, confirming that our protocol efficiently pulled down PUM1 protein from both patient-derived cell lines (Supplemental Figure 13C and D).

Co-IP confirmed that PUM1 associates with FMRP, AGO2, CNOT1, and MOV10 in patient cell lines (Supplemental Figure 13A and B). The mild T1035S variant reduced PUM1 binding to AGO2 but this was not significant (Supplemental Figure 13D). The more severe R1147W, however, reduced PUM1 association with AGO2, CNOT1, and MOV10 by ~84%, ~59%, and ~90%, respectively (Supplemental Figure 13A). Interaction with FMRP did not appear to be affected. (We could not examine the effect of PUM1 mutations on RBFOX3, which is not expressed in fibroblasts or lymphoblastoid cells.)

To compare the mutants in the same cell type, we turned to HEK293T cells. We found that GST-AGO2 associated with Myc-PUM1-R1147W 72% less than it did with Myc-PUM1-WT (Figure 6A), in alignment with our observations in the PADDAS cell lines (Supplemental Figure 13A and B). We also found ~35% less interaction with CNOT1 (Figure 6B) but no decrease in PUM1 association with FMRP (Figure 6C), again in accord with our findings in patient-derived cells (Supplemental Figure 13A and B).

We next asked whether the R1147W mutation might be impaired in binding with WT PUM1. We found that IP against Myc-PUM1-R1147W pulled down 51% of the total GST-PUM1-WT, while the interaction between Myc-PUM1-T1035S and GST-PUM1-WT remained unchanged (Figure 6D). The same interaction was observed after RNase treatment, suggesting that mammalian PUM1 interacts with itself in the absence of RNA (Supplemental Figure 14A). These data suggest that the R1147W mutation might exert a dominant-negative effect on WT PUM1. Moreover, the combination of lower protein levels and marked protein instability explains why the R1147W human phenotype is closer to that of the *Pum1* null mice than to the heterozygous mice (10).

To confirm that R1147W destabilizes PUM1 interactors, we quantified the protein levels of these RBPs from patient-derived cell lines. This analysis revealed that the proteins that lose their association with the R1147W variant also are reduced in their expression (Figure 6E). Note that MOV10's association with R1147W was greatly reduced (Supplemental Figure 13A) even though its protein levels were unchanged (Figure 6E). AGO2 and CNOT1 levels were unchanged in the PRCA cell line but were ~50%

lower in the PADDAS cell line (Figure 6E). The mRNA levels of *PUM1*, *AGO2*, *CNOT1*, and *MOV10* did not change (Supplemental Figure 14B), confirming that the reductions in their respective protein levels were due to the loss of interaction with PUM1-R1147W. These data suggest that the R1147W variant might also exert a dominant-negative effect on PUM1-RBP interactors by destabilizing them.

Shared targets are upregulated in PADDAS but not PRCA

We had hypothesized that PRCA involves dysregulation of PUM1 targets, whereas PADDAS involves both destabilization of PUM1 interactors and dysregulation of their targets. We therefore tested the effects of the T1035S and R1147W mutations on both shared targets and validated PUM1-specific targets (11, 24, 53) that are not in the HITS-CLIP data for the other RBPs but are expressed in both fibroblasts and lymphoblasts. PUM1-specific mRNA were dysregulated to very similar extents in PRCA and PADDAS patient cells, with only a few targets being up to 20% more upregulated in PADDAS (Supplemental Figure 14C).

Of the 175 targets shared between PUM1, PUM2, AGO2, FMRP, and RBFOX3 (Figure 5E and Supplemental Table 5), 54 were expressed in both PADDAS fibroblasts and PRCA lymphoblastoid cells. Fifty-one of those were upregulated in PADDAS but not in PRCA (Figure 7A), by an average of two-fold (ranging from a low of 121% for *IDS* to 347% for *TLK1*). There was little or no change in most of these targets in PRCA cells, though levels of *CALM1*, *ATP2A2*, *CREB1*, and *GNAQ* fell by ~40%, and *CALM2*, *TAOK1*, and *UBE2A* by ~20% (Figure 7A).

Finally, we tested whether restoring PUM1 levels would normalize expression of these shared targets. Transfection of Myc-PUM1-WT in PADDAS cells (Figure 7B, and Supplemental Figure 14D) rescued AGO2 and CNOT1 protein levels compared to the age- and sex-matched healthy controls (transfection with an empty vector was used here as negative control) (Figure 7B). Moreover, this reduced the levels of the top 15 upregulated shared targets. These data confirm that the effects of the R1147W mutation, which does not impair PUM1 binding to mRNA (10), result from loss of interactions with RBPs that repress the same mRNA targets. These results also support the hypothesis that the symptoms observed in PRCA are attributable to the dysregulation of PUM1-specific target genes, while PADDAS involves both protein partner destabilization and dysregulation of the partner proteins' targets.

Discussion

Since our initial study describing PUM1-related diseases (10), we and others have identified additional PADDAS and PRCA patients (10, 54-56). In our cohort, the R1147W mutation accounts for the majority of PADDAS patients, and T1035S for the majority of PRCA, which supports the value of

studying these particular two mutations. The question that drove the present study is: why should the additional 25% drop in PUM1 levels from PRCA to PADDAS produce such different phenotypes, especially when R1147W is not impaired in binding to mRNA? Our data support the hypothesis that the difference is not due to a linear increase in the de-repression of mRNA targets but is rather a function of an additional mechanism coming into play: the destabilization of numerous interactors and the de-repression of their downstream targets. This conclusion relies on five lines of evidence. First, loss of Pum1 in heterozygous and knockout mice changes the levels of associated proteins, with unexpected differences emerging between brain regions and between male and female mice. These differences involved exchanges between members of the same protein families (e.g., the Rbfox family). The odds of consistently identifying specific proteins in different brain regions and sexes as false positives, across as many mice as these experiments required, are extremely low. Second, we observed diminished function of the RBP interactors in the absence of Pum1, insofar as their targets are dysregulated in Pum1-KO mice; moreover, the dysregulation of miRNA showed opposite patterns in male and female cerebella that correlated with the sex-specific patterns of Ago2 expression. Third, the levels of these proteins were reduced 40-70% in PADDAS patient cell lines, despite unaltered mRNA levels, but not in PRCA patient cells; we also found that 55 shared targets expressed in both lymphoblasts and fibroblasts were derepressed in PADDAS, but not PRCA, cells. Fourth, our *in vitro* studies showed that AGO2 and CNOT1 lose their interaction with PUM1-R1147W. Fifth, re-expression of PUM1 in PADDAS cell lines rescued the levels of its interactors and restored suppression of downstream shared targets. In aggregate, these data suggest that a ~50% loss of PUM1 disrupts interactions with native partners, differentiating PADDAS from PRCA. These results underscore the importance of examining RBP interactions *in vivo*, in specific contexts (different sex or brain regions), with and without RNase treatment.

There are other dosage-sensitive proteins that produce different phenotypes depending on their expression level (57), and our results raise the possibility that interacting complexes may be disrupted once expression falls below a certain threshold. What that threshold might be likely differs for different proteins, but for PUM1 it seems to be somewhere between the 75% of wild-type levels of PUM1 seen in PRCA and the 60% level estimated for the R1139W mutation that produced a milder form of PADDAS (10). In this context it is worth noting that a recent study found that, below a threshold of ~70% of normal levels of FMRP, there were steep decreases in IQ for each further decrement in FMRP levels, even as small as 5-10% (58). The amount of loss that can be sustained for a given protein would likely depend on its usual quantities, and it is possible that for some proteins, the difference in phenotype between greater and lesser abundance may indeed reflect a linear progression from mild to severe. For example, in proteopathies such as Alzheimer's or Parkinson's disease, genetic duplications of *APP* or *SNCA* cause an

earlier onset of what is recognizably the same disease (59, 60). Similarly, a mutation in *MECP2* that reduces its protein levels by only 16% is still sufficient to cause a mild form of Rett syndrome (61).

In contrast, there are diseases in which the phenotypes do not simply range from mild to severe versions of the same symptoms, but seem to take on a different character. In the polyglutaminopathies, the disease-causing protein bears an abnormally expanded CAG tract that tends to expand upon intergenerational transmission. Although the range of normal and pathogenic repeat tract lengths differs from one polyglutamine disease to another, larger expansions are more unstable, cause earlier onset, and affect far more tissues than smaller expansions (62). For example, adult-onset SCA7 presents as ataxia, but infantile SCA7 affects the entire nervous system, the heart, and the kidneys, and leads to death by two years of age (63). Another example is Huntington's disease (HD), where the juvenile form frequently lacks the classic chorea yet produces seizures, which are not a feature of the adult-onset disease; brain morphometry is also quite different in adult- and juvenile-onset cases (64). In this family of diseases, therefore, the mechanism is the same (repeat expansion), but different tissues have different thresholds for the CAG repeats. Moreover, the brain regions most vulnerable to HD show dramatic levels of somatic instability that correlate better with clinical outcomes than the germline polyglutamine expansion (65, 66).

In the case of PUM1-related disease, it seems that an additional mechanism comes into play for the more severe phenotypes, beyond upregulation of mRNA targets. Interestingly, FMRP, which harbors a dynamic CGG repeat, is also associated with very different diseases, through two different mechanisms. Very large expansions silence the gene and produce Fragile X syndrome, whereas premutations are thought to cause the adult-onset Fragile-X-associated tremor/ataxia syndrome through RNA toxicity (FXTAS) (67). Interestingly, the clinical presentation of FXTAS differs by sex. We have more females with PUM1 mutations in our cohort, but with only 60 patients the sample is too small to draw any conclusions about the influence of sex on either the PADDAS or PRCA phenotype.

There are several limitations to this study. The most notable is that it is difficult to demonstrate direction interactions *in vivo*, and it is theoretically possible that we could be seeing post-lysis interactions. However, we examined the interactions in different brain regions where the two proteins of interest are equally expressed, and we repeatedly identified interactions that were consistently restricted to certain regions, such as with Pum2. A mere post-lysis interaction cannot be specific to a particular brain region or sex, especially with as many biological replicates as we have performed. We also had only three patient cell lines to test (one PADDAS, two PRCA), and lymphoblasts and fibroblasts are not directly comparable; they are also not neurons. Nevertheless, both fibroblasts and lymphoblasts express almost one-third of the shared targets we identified in mouse brains, and these were clearly dysregulated

in both cell types. Moreover, we replicated the patient-derived cell line results *in vitro* with tagged proteins. Future studies in iPSC-derived neurons would be useful, although the neuronal type and the sex of the patient would have to be taken into account.

Despite these clear limitations, our data suggest some provocative possibilities for future investigation. It has never been clear how the various modes of action attributed to PUM1 or other RBPs relate to one another. Our data suggest that the three mechanisms of repression that have been proposed for PUM1—collaborating with the miRNA machinery (12-14), recruiting the CCR4-NOT deadenylase complex to trigger degradation (15-17), and antagonizing poly(A)-binding proteins to repress translation (18)—might be coordinated in neurons, insofar as PUM1, PUM2, FMRP, AGO2, MOV10, CNOT1 and RBFOX3 (and related proteins in specific brain regions) either interact or are so close to each other within the ribonucleosome that the loss of Pum1 or RNA can change the composition of the complexes that are identified by co-IP, in ways that are specific to brain region and sex. In this context it is worth noting that a very recent study found alternative splicing is altered in hippocampal slices from Fmrp-deficient mice; this observation was attributed to changes in H3K36me3 levels (68), but our data suggest that FMRP has a closer relationship with the RBFOX protein family and alternative splicing machinery. Indeed, recent work has provided tantalizing glimpses of close interactions among various kinds of RNA metabolism. For example, members of the RBFOX family of proteins may, depending on their interactors (and perhaps cell type, sex, age, and species), be involved in microRNA processing in the nucleus and translation in the cytoplasm (69). The FMRP/MOV10 complex appears to be involved in regulating translation through miRNA, with evidence that this role may change according to cell type (29). Another study used quantitative mass spectroscopy to examine how Fmrp expression levels change with age in the wild-type rat dentate gyrus, and found differences in the levels of myriad proteins; among the 153 proteins with the most significant changes in levels were Pum1, Pum2 and Papbc1 (70). The region-, sex-, and age-specificity of certain interactions indicates that unraveling RBP interactomes *in vivo* will require considerable finesse. But creating such interactomes should lead to a more complex yet realistic picture of RBP roles in neuronal function and in neurological disease.

Acknowledgments

We thank the patients, their families, and their clinical teams for participating in our study, and the anonymous reviewers for helpful suggestions. We thank Mingyu Cao for help with statistical analyses and U.N. Wasko for starting the cloning procedure with Myc and GST tag sequences *in vitro*. We also thank G. Struhl, V. Ambros, T. Duchaine, G. Karsenty, H. Zoghbi, M. Jovanovic, Y. Giardina, V. Brandt,

and members of the Gennarino laboratory for helpful discussions and support. This work was supported by the National Institute of Neurological Disorders and Stroke (NINDS; R01NS109858 to V.A.G.); the National Ataxia Foundation/Young Investigator Research Grant (V.A.G.); the Brain & Behavior Research Foundation Young Investigator Award; and the Paul A. Marks Scholar Program, Columbia University Vagelos College of Physicians and Surgeons. The authors declare no competing interests.

Author contributions

S.B. designed and performed molecular experiments, analyzed and interpreted the data, and drafted the manuscript. N.D.P. performed the qPCR experiments, *in vitro* immunoprecipitation assays, analyzed the data, and edited the manuscript. A.C. performed all the brain region dissections in mice, performed the qPCR experiments and maintained the *Pum1* mutant mouse colony. M.C. performed the cloning experiments. P.P and R.K.S. performed mass spectrometry and helped analyze the data. V.A.G. conceived the study, analyzed and interpreted the data, performed molecular experiments, and wrote the manuscript.

Declaration of Interests

The authors declare not competing interests

Figures (start on next page)

Figure 1

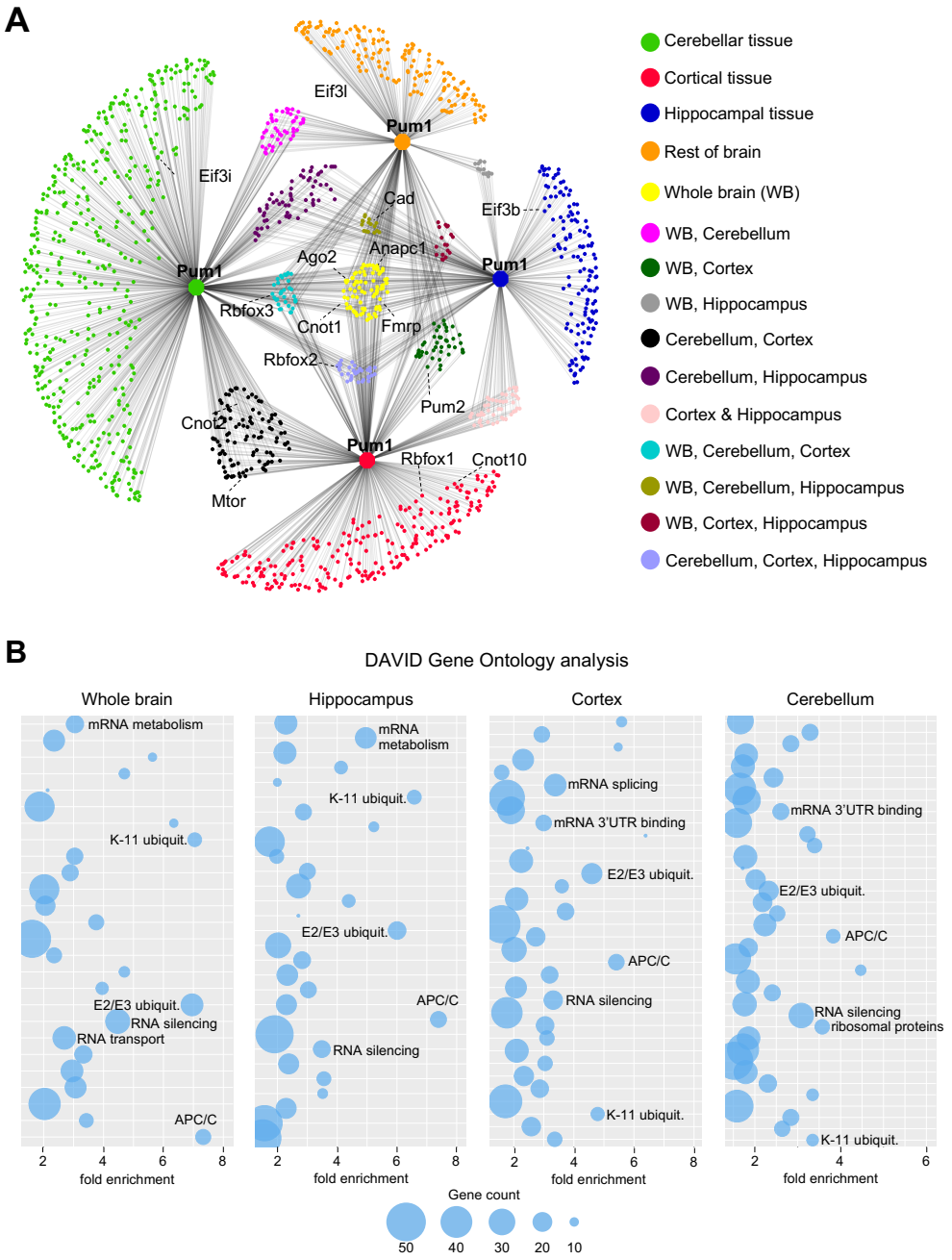

Figure 1. A brain-region specific Pum1 interactome. (**A**) Pum1 interactome from 10-week-old mouse cerebellum (n=8 mice, 4 male and 4 female), hippocampus (n=10, 5/5), cortex (n=8, 4/4) and the rest of the brain (i.e., excluding those three regions) for a total of 1,500 proteins (Supplemental Table 1). Node colors represent different brain regions or the overlap between two or more brain regions as noted. All experiments were performed at least in triplicate. IP against IgG was used as a negative control. (**B**)

Bubble plots show the top categories from gene ontology analyses of Pum1 interactors from whole brain, hippocampus, cortex, and cerebellum. Only the categories with fold enrichment >1.5 and FDR<0.05 are shown; not all are labeled because of space limitations. The full list of gene ontology categories is available in Supplemental Table 2.

Figure 2

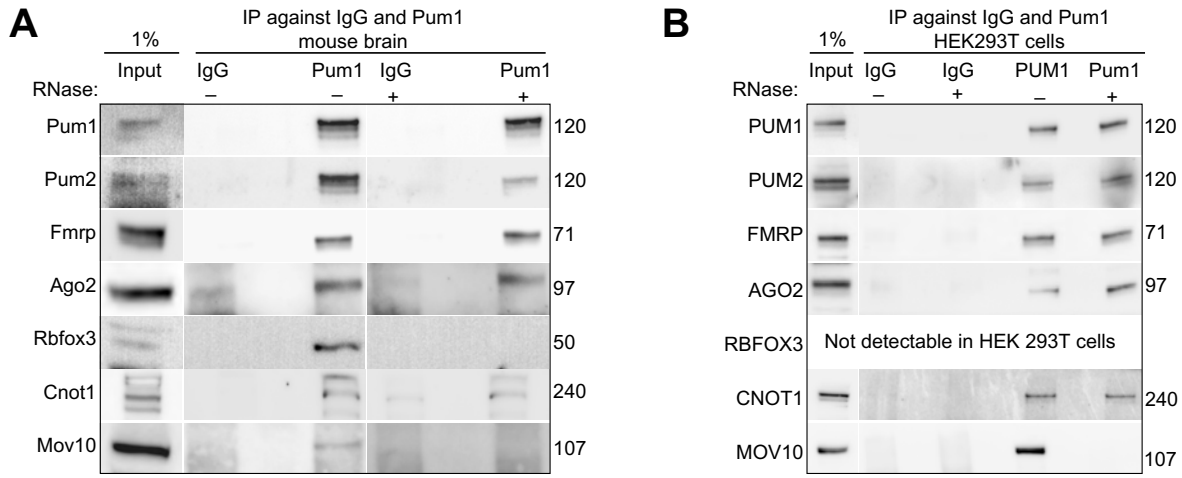

Figure 2. Validation of Pum1 associations with post-transcriptional RNA-binding proteins in mouse brain and HEK293T cells. (**A**) Representative western blot of proteins pulled down by IP against Pum1 compared to IgG from wild-type mice brain without (*left*) and with (*right*) RNase treatment. In this panel, after IP-Pum1, we immunoblotted for Pum1 (positive control), Pum2, Fmrp, Ago2, Rbfox3, Cnot1, and Mov10. (see Methods.). (**B**) Representative western blots of the same proteins validated in panels **A** after IP against PUM1 with or without RNase treatment from HEK293T cell lines. In panels **A** and **B**, IP against IgG was used as a negative control and Input (1% from the initial protein lysate) as a loading control. The numbers on the right are the respective molecular weights expressed in kilodaltons (kDa). All the experiments were repeated at least four times. All mice were sacrificed at 10 weeks of age.

Figure 3

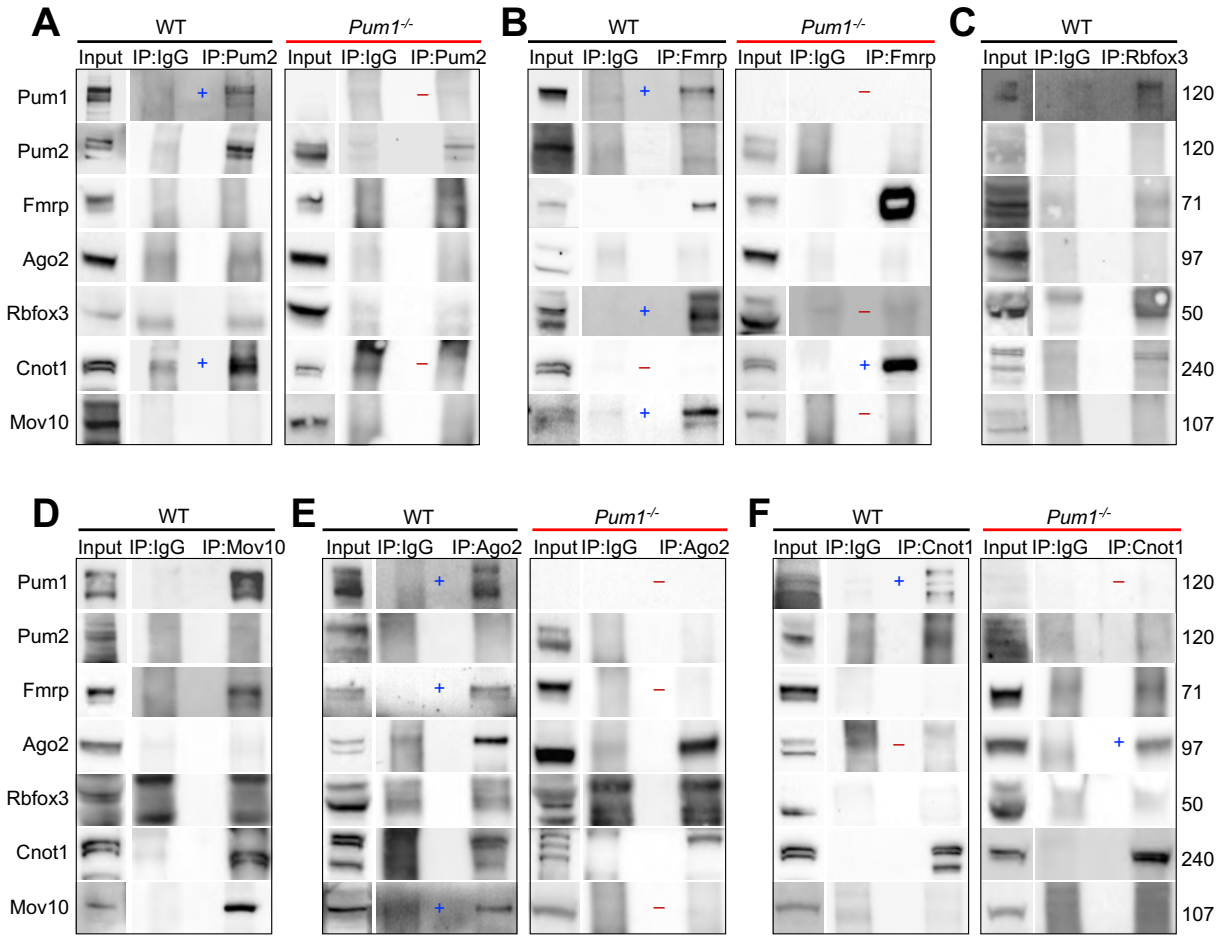

Figure 3. Effects of Pum1 loss on interactions among the six RNA-binding proteins. Representative western blot of the proteins pulled down by (**A**) Pum2, (**B**) Fmrp, (**C**) Rbfox3, (**D**) Mov10, (**E**) Ago2, and (**F**) Cnot1 from WT and *Pum1*$^{-/-}$ mouse brain at 10 weeks of age. IP against IgG was used as a negative control, and Input (1% from the initial protein lysate) as a loading control. Molecular weights to the right are expressed in kilodaltons (kDa). All the experiments were repeated at least three times. Since Rbfox3 and Mov10 interactions with Pum1 are RNA-dependent we did not perform IP from *Pum1*$^{-/-}$ mouse brain.

Figure 4

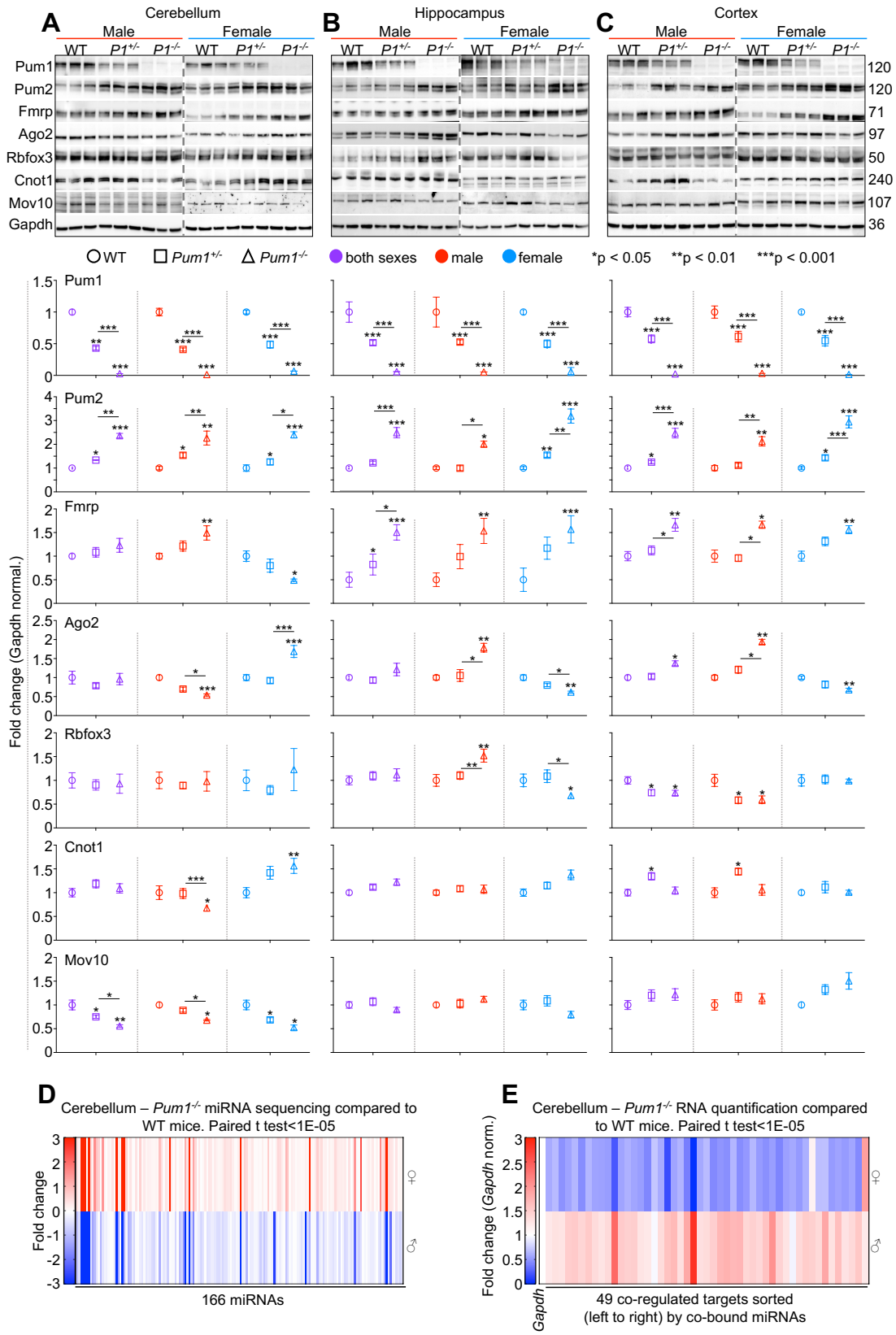
A
Cerebellum
B
Hippocampus
C
Cortex
Male
Female
WT
P1+/-
P1-/-
Pum1
Pum2
Fmrp
Ago2
Rbfox3
Cnot1
Mov10
Gapdh
120
120
71
97
50
240
107
36
WT
Pum1+/-
Pum1-/-
both sexes
male
female
*p < 0.05
**p < 0.01
***p < 0.001
Fold change (Gapdh normal.)
D
Cerebellum – Pum1-/- miRNA sequencing compared to WT mice. Paired t test<1E-05
Fold change
166 miRNAs
E
Cerebellum – Pum1-/- RNA quantification compared to WT mice. Paired t test<1E-05
Fold change (Gapdh norm.)
Gapdh
49 co-regulated targets sorted (left to right) by co-bound miRNAs

Figure 4. Pum1 interactors and the microRNA machinery show brain region- and sex-specific responses to Pum1 loss. Representative western blots of Pum1, Pum2, Fmrp, Ago2, Rbfox3, Cnot1, and Mov10 in (**A**) cerebellum, (**B**) hippocampus, and (**C**) cortex in both male (left panel) and female (right panel) WT, *Pum1*$^{+/-}$, and *Pum1*$^{-/-}$ mice. All the experiments were conducted with equal numbers of 10-week-old male and female mice per genotype, for a total of at least 12 mice per genotype (data represent mean ± SEM). Graphs below show quantification for each protein by brain region, sex, and genotype. All data were normalized to Gapdh protein levels. Data represent mean ± SEM. P values were calculated by two-tailed Student's t test. *$p < 0.05$, **$p < 0.01$, ***$p < 0.001$. P1 indicates Pum1. See Supplemental Figure 8 for mRNA quantification for each interactor, brain region, and sex. (**D**) Heatmap showing 166 microRNAs from cerebella of *Pum1*$^{-/-}$ male and female mice that were dysregulated (fold change -3 to +3) relative to wild-type cerebellum. The full list of miRNA names and fold changes are available in Supplemental Table 3. See Supplemental Figure 9 for male and female miRNA scatter plots. (**E**) Heatmap showing mRNA quantification by qPCR for 49 targets co-bound by a minimum of eight dysregulated miRNAs (>25% change) from panel **D**. For **D** and **E,** three cerebella per genotype and sex were analyzed. Statistical significance and magnitude of dysregulation are illustrated for both male and female in Supplemental Figure 10. The entire list of targets predicted to be co-bound by at least two miRNAs is presented in Supplemental Table 4.

Figure 5

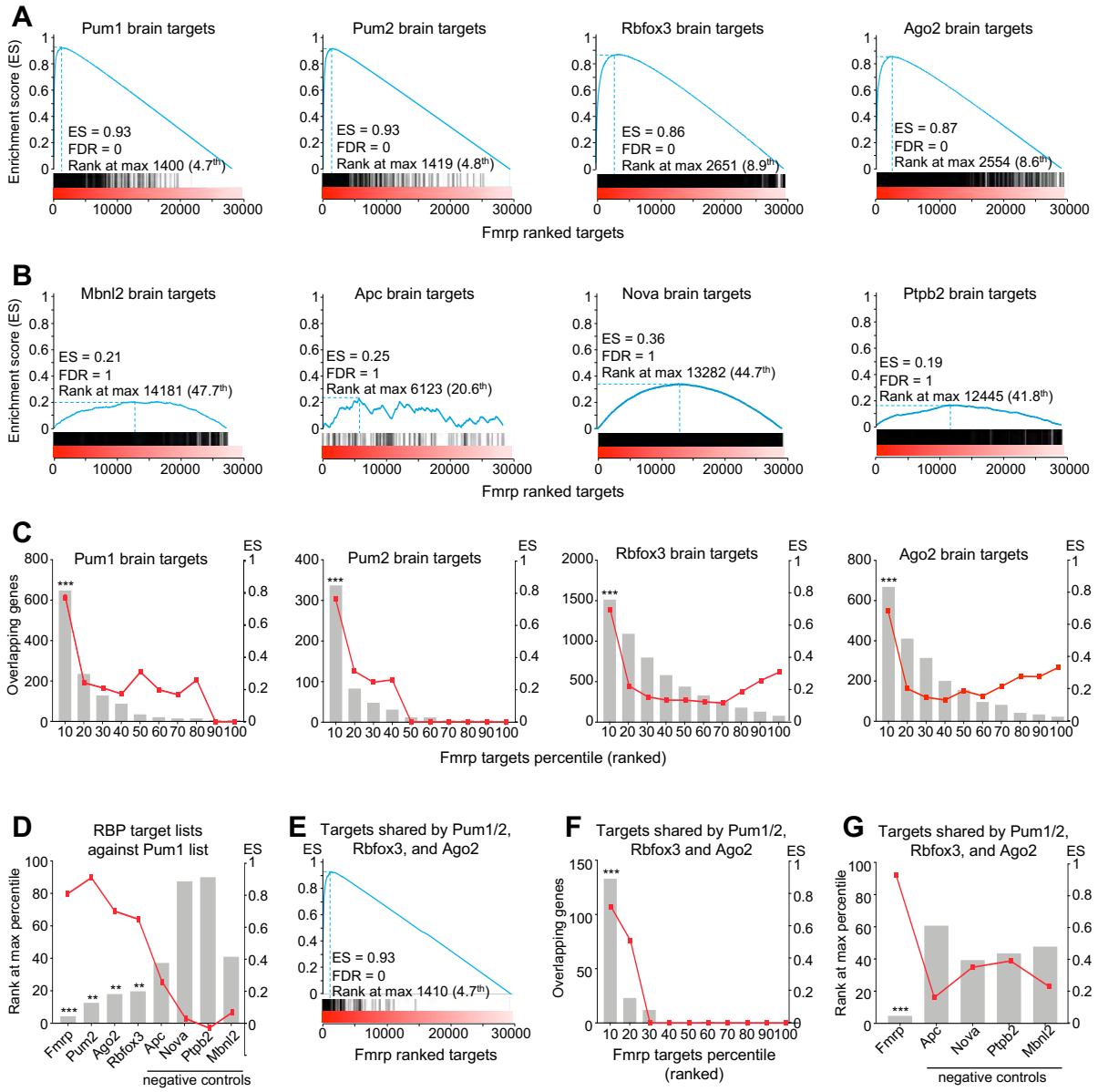

Figure 5. Pum1 and its RNA-binding protein interactors share many neuronal mRNA targets. (**A**) Enrichment plots generated by Gene Set Enrichment Analysis (GSEA) of Pum1, Pum2, Rbfox3, and Ago2 HITS-CLIP targets plotted again Fmrp ranked HITS-CLIP data. Pum1, Pum2, Rbfox3, and Ago2 targets are enriched at the top 10th percentile of the Fmrp targets with FDR=0. (**B**) GSEA analysis scores of HITS-CLIP data from each negative control (Apc, Nova, Ptpb2, and Mbnl2) plotted against Fmrp ranked HITS-CLIP data. The negative controls have a maximum enrichment score of 0.36 for Apc

ranking at the top 44.7% with FDR=1. (**C**) GSEA analysis scores of Pum1, Pum2, Rbfox3, and Ago2 HITS-CLIP data plotted against Fmrp HITS-CLIP data divided into 10-percentile ranked bins shows the shared targets are among the top percentiles of targets for each protein. (**D**) GSEA analysis scores of the HITS-CLIP data for Fmrp, Pum2, Ago2, Rbfox3 and four negative controls (Apc, Nova, Ptpb2, and Mbnl2) against Pum1 ranked HITS-CLIP data. The targets of Fmrp, Ago2, Pum2, and Rbfox3 are enriched at the top 5^{th} to 18^{th} percentile of Pum1 targets. (**E**) GSEA analysis of the shared targets between Pum1, Pum2, Ago2, and Rbfox3 against Fmrp showing that they are enriched in the top 5^{th} percentile of Fmrp ranked targets. (**F**) Pum1, Pum2, Ago2, and Rbfox3 shared targets plotted against Fmrp ranked HITS-CLIP targets and divided into 10-percentile bins shows that all of their respective targets are enriched at the top 10^{th} percentile of the Fmrp ranked targets. (**G**) GSEA analysis scores of the targets shared by Pum1, Pum2, Ago2, and Rbfox3 and the four negative controls (Apc, Nova, Ptpb2, and Mbnl2) plotted against Fmrp. At best the negative controls are enriched at the top 40% with a maximum ES of 0.41. For all the GSEA analyses, the False Discovery Rate (FDR) was provided by GSEA: **FDR<0.05 and ***FDR<0.01. ES=Enrichment score (blue line). Note that lowest rank at max percentage indicates stronger targets in the rank (see Methods). HITS-CLIP data, and the respective rank, were obtained from the literature and were initially acquired as follows: Pum1 and Pum2 (24), Fmrp (45), Ago2 (46), Rbfox3 (47), Nova (50), Ptpb2 (52), Mbnl2 (49), and Apc (51) (see Methods for more details). The full list of shared targets is reported in Supplemental Table 5.

Figure 6

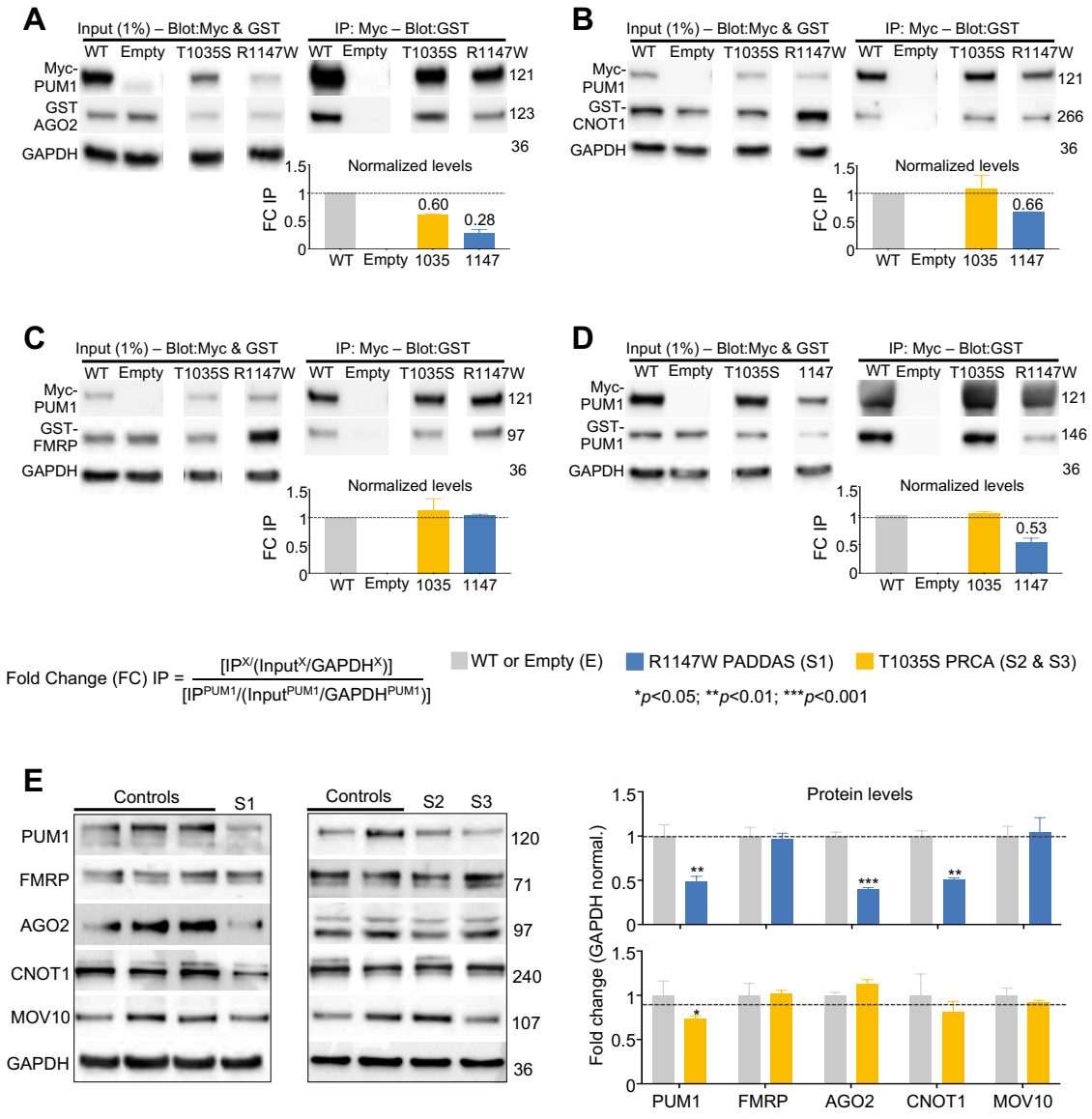

Figure 6. The R1147W mutation, but not T1035S, destabilizes PUM1 interactors. (**A-D**) Representative western blots and relative IP quantification (*bar graphs*) of IP against Myc-PUM1-WT, Myc-PUM1-T1035S (PRCA), or Myc-PUM1-R1147W (PADDAS) followed by immunoblotting for: (**A**) GST-AGO2, (**B**) GST-CNOT1, (**C**) GST-FMRP, and (**D**) GST-PUM1-WT. Myc- and GST-tagged proteins were co-transfected in HEK293T cells in equal quantities (250ng each). The molecular weights were expressed in kilodaltons (kDa). The amount of protein pulled down compared to IP-PUM1 was quantified as $[IP^{X}/(Input^{X}/GAPDH^{X})]/ [IP^{PUM1}/(Input^{PUM1}/ GAPDH^{PUM1})]$, where X is the protein of

interest. (**E**) Representative western blots (*left panels*) and relative quantification (*bar graphs to the right*) of protein levels for PUM1, PUM2, FMRP, AGO2, CNOT1, and MOV10 in PADDAS patient-derived fibroblasts and PRCA patient-derived lymphoblastoid cells compared to their respective age- and sex-matched fibroblast (for PADDAS patients) and lymphoblastoid (for PRCA patients) controls. Data were normalized to Gapdh protein levels. From **A** to **E,** all the experiments were performed at least three times. Data represent mean ± SEM. P values were calculated by two-tailed Student's t test. *$p < 0.05$, **$p < 0.01$, ***$p < 0.001$.

Figure 7

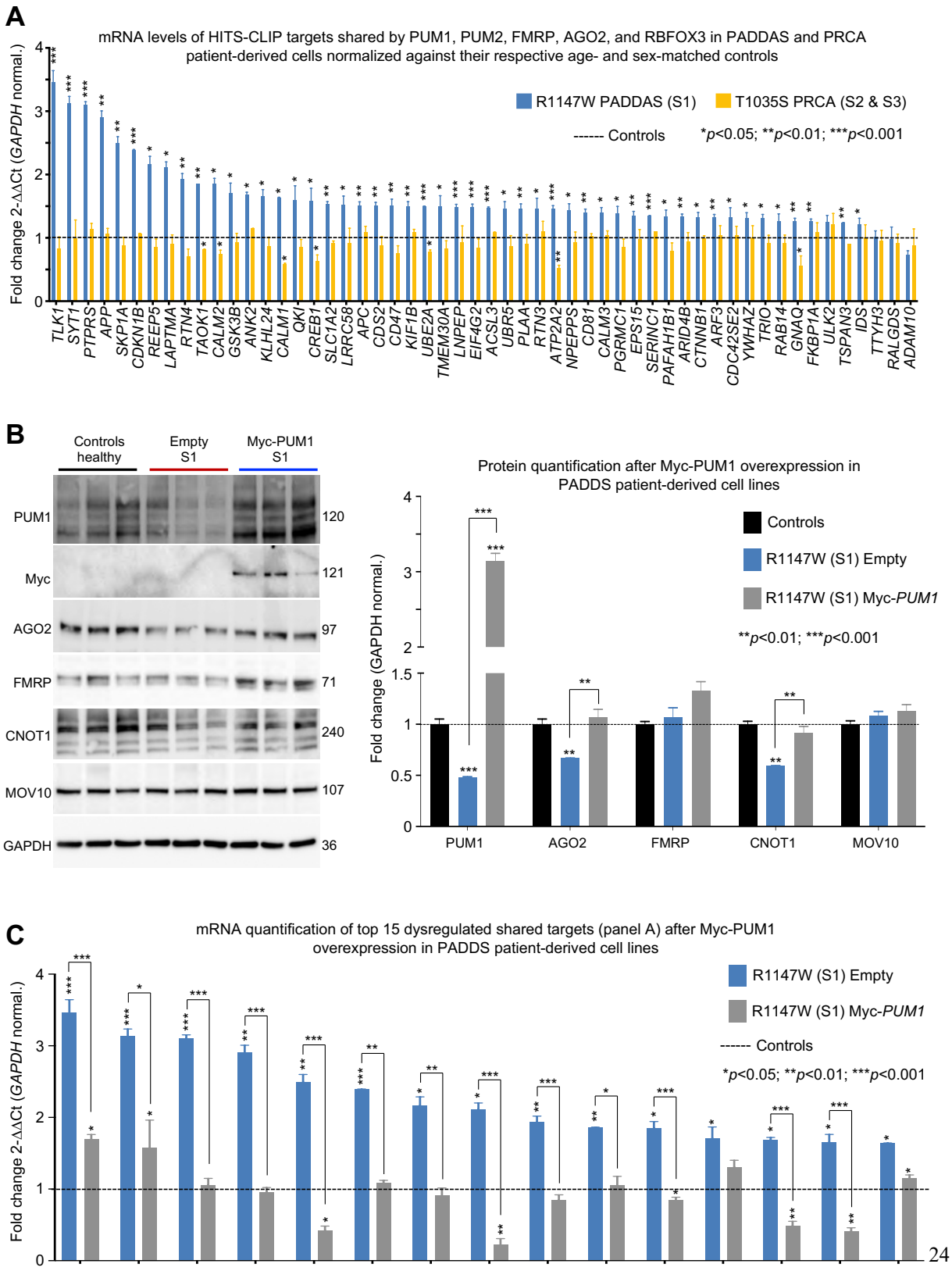
A
mRNA levels of HITS-CLIP targets shared by PUM1, PUM2, FMRP, AGO2, and RBFOX3 in PADDAS and PRCA patient-derived cells normalized against their respective age- and sex-matched controls
R1147W PADDAS (S1)
T1035S PRCA (S2 & S3)
------ Controls
*p<0.05; **p<0.01; ***p<0.001
Fold change 2-ΔΔCt (GAPDH normal.)
TLK1 SYT1 PTPRS APP SKP1A CDKN1B REEP5 LAPTMA RTN4 TAOK1 CALM2 GSK3B ANK2 KLHL24 CALM1 QKI CREB1 SLC1A2 LRRC58 APC CDS2 CD47 KIF1B UBE2A TMEM30A LNPEP EIF4G2 ACSL3 UBR5 PLAA RTN3 ATP2A2 NPEPPS CD81 CALM3 PGRMC1 EPS15 SERINC1 PAFAH1B1 ARID4B CTNNB1 ARF3 CDC42SE2 YWHAZ TRIO RAB14 GNAQ FKBP1A ULK2 TSPAN3 IDS TTYH3 RALGDS ADAM10
B
Controls healthy
Empty S1
Myc-PUM1 S1
PUM1 120
Myc 121
AGO2 97
FMRP 71
CNOT1 240
MOV10 107
GAPDH 36
Protein quantification after Myc-PUM1 overexpression in PADDS patient-derived cell lines
Controls
R1147W (S1) Empty
R1147W (S1) Myc-PUM1
**p<0.01; ***p<0.001
Fold change (GAPDH normal.)
PUM1 AGO2 FMRP CNOT1 MOV10
C
mRNA quantification of top 15 dysregulated shared targets (panel A) after Myc-PUM1 overexpression in PADDS patient-derived cell lines
R1147W (S1) Empty
R1147W (S1) Myc-PUM1
------ Controls
*p<0.05; **p<0.01; ***p<0.001
Fold change 2-ΔΔCt (GAPDH normal.)

550

Figure 7. Shared targets are upregulated only in PADDAS, not in PRCA. (**A**) mRNA level quantification of PUM1 neuronal targets in common with FMRP, PUM2, AGO2, and RBFOX3 (Figure 5E and Supplemental Table 5) in fibroblasts from subject 1 (PADDAS patient, R1147W) compared to the three age- and sex-matched control fibroblast lines (blue bars), and in lymphoblastoid cells from subjects 2 and 3 (PRCA patients, T1035S) compared to the three age- and sex-matched control lymphoblastoid cell lines (orange bars). Only genes expressed in both fibroblasts and lymphoblasts are represented here for a total of 54 genes. (**B**) Representative western blots (*right panel*) and relative quantifications (*left panel*) of PUM1 and its interactors (AGO2, CNOT1, FMRP, and MOV10) in PADDAS fibroblast patient-derived cell lines after Myc-PUM1-WT expression. (**C**) mRNA quantification of the top 15 shared target genes from panel **A** in PADDAS fibroblast patient-derived cell lines after Myc-PUM1-WT expression. All data were normalized to GAPDH mRNA or protein levels and experiments were performed at least three times. Data represent mean ± SEM. P values were calculated by two-tailed Student's t test. *$p < 0.05$, **$p < 0.01$, ***$p < 0.001$. The full list of shared targets expressed in fibroblast and lymphoblast cell lines is reported in Supplemental Table 5.

Methods

A detailed description is found in the Supplemental Methods.

Ethical statement and mouse strains. All animal procedures were approved by the Institutional Animal Care and Use Committee at Columbia University, New York under the protocol AC-AAAU8490. Mice were maintained on a 12-hr light, 12-hr dark cycle with regular chow and water ad libitum. Pum1 knock-out mice were generated as previously described (53). C57BL/6J wild-type mice were purchased from Jackson Laboratory and maintained as described above. For brain dissection, mice were anesthetized with isoflurane, and the brain rapidly removed from the skull and lysed in the appropriate buffer according to the experiment (see Materials and Methods Details).

Experimental design. For protein and RNA quantification from patient-derived cell lines, we used values from at least six independent experiments with three biological replicates for each experiment. At every stage of the study, the experimenter was blinded to the identity of control and patient-derived cell lines. For example, for the data regarding both human patient-derived cell lines and mice, Experimenter #1 made a list of samples and controls to be tested, and Experimenter #2 randomized this list and re-labeled the tubes; Experimenter #2 was the only person with the key to identify the samples. These samples were then distributed to Experimenter #3 to culture the cells, then to Experimenter #1 to perform western blots

584 and qRT-PCR, and lastly Experimenters #1 and #4 analyzed the data. Only then was the key applied to
585 identify the samples.
586 For mouse experiments, the experimenters were randomized and blinded as described above. The
587 number of animals used and sex, and the specific statistical tests used, are indicated for each experiment
588 in the figure legends. Sample size was based on previous experience using the same mice (11).
589
590 **Software and statistical analysis.** Statistical significance was analyzed using GraphPad Prism 8
591 (https://www.graphpad.com/ scientific-software/prism/) and Excel Software (Microsoft). All data are
592 presented as mean ± SEM. Statistical details for each experiment can be found in the figures and the
593 legends. The range of expression levels in qPCR was determined from at least six independent
594 experiments with three biological replicates by calculating the standard deviation of the **Δ**Ct (71). The
595 range of expression levels in western blots was determined from at least six independent experiments with
596 at least six biological replicates. P values were calculated by Student's T-test or analysis of variance with
597 Tukey's post hoc analysis. For the IP and protein quantification in patient cell lines in Figure 6E and
598 Supplemental Figure 13A and B, we had only one PADDAS patient, so the repeated experiments were
599 technical replicates rather than biological replicates. We therefore calculated the statistical significance
600 based on these technical replicates in comparison to the three biological replicates (i.e., healthy controls).
601
602 **Study approval.** PADDAS and PRCA patient cell lines are the same as those reported previously (10).
603 The consent form for each subject specifically allows for sharing of medical information and physical
604 exam findings; the sharing of cell lines from the PADDAS and PRCA subjects and the controls was
605 approved under the Columbia University Medical Center IRB-AAAS7401 (Y01M00) and the Baylor
606 College of Medicine IRB H-34578.
607

608 ## Data Availability

609 **Materials and reagents.** Further information and requests for resources, reagents, and mouse models
610 used in this manuscript should be directed to and will be fulfilled by Vincenzo A. Gennarino
611 (vag2138@cumc.columbia.edu).
612
613 **Code and raw data.** No software was generated for this project. All software used in this study is
614 publicly available and links are provided as appropriate in different sections of the Materials and
615 Methods. Mass spectrometry, RNA sequencing and microRNA sequencing raw data generated during this
616 study are available at PRIDE Archive at https://www.ebi.ac.uk/pride/archive, and Gene Expression

Omnibus (GEO) at https://www.ncbi.nlm.nih.gov/geo/ with the accession numbers pending.

References

1. Hentze MW, Castello A, Schwarzl T, and Preiss T. A brave new world of RNA-binding proteins. *Nat Rev Mol Cell Biol.* 2018;19(5):327-41.
2. Keene JD. RNA regulons: coordination of post-transcriptional events. *Nat Rev Genet.* 2007;8(7):533-43.
3. Dassi E. Handshakes and Fights: The Regulatory Interplay of RNA-Binding Proteins. *Front Mol Biosci.* 2017;4:67.
4. Mauger O, Lemoine F, and Scheiffele P. Targeted Intron Retention and Excision for Rapid Gene Regulation in Response to Neuronal Activity. *Neuron.* 2016;92(6):1266-78.
5. Lukong KE, Chang KW, Khandjian EW, and Richard S. RNA-binding proteins in human genetic disease. *Trends Genet.* 2008;24(8):416-25.
6. Humphrey J, Birsa N, Milioto C, McLaughlin M, Ule AM, Robaldo D, et al. FUS ALS-causative mutations impair FUS autoregulation and splicing factor networks through intron retention. *Nucleic Acids Res.* 2020;48(12):6889-905.
7. Ravanidis S, Kattan FG, and Doxakis E. Unraveling the Pathways to Neuronal Homeostasis and Disease: Mechanistic Insights into the Role of RNA-Binding Proteins and Associated Factors. *Int J Mol Sci.* 2018;19(8).
8. Darnell JC, and Richter JD. Cytoplasmic RNA-binding proteins and the control of complex brain function. *Cold Spring Harb Perspect Biol.* 2012;4(8):a012344.
9. Khalil B, Morderer D, Price PL, Liu F, and Rossoll W. mRNP assembly, axonal transport, and local translation in neurodegenerative diseases. *Brain Res.* 2018;1693(Pt A):75-91.
10. Gennarino VA, Palmer EE, McDonell LM, Wang L, Adamski CJ, Koire A, et al. A mild PUM1 mutation is associated with adult-onset ataxia, whereas haploinsufficiency causes developmental delay and seizures. *Cell.* 2018;172(5):924-36 e11.
11. Gennarino VA, Singh RK, White JJ, De Maio A, Han K, Kim JY, et al. Pumilio1 haploinsufficiency leads to SCA1-like neurodegeneration by increasing wild-type Ataxin1 levels. *Cell.* 2015;160(6):1087-98.
12. Friend K, Campbell ZT, Cooke A, Kroll-Conner P, Wickens MP, and Kimble J. A conserved PUF-Ago-eEF1A complex attenuates translation elongation. *Nat Struct Mol Biol.* 2012;19(2):176-83.
13. Kedde M, van Kouwenhove M, Zwart W, Oude Vrielink JA, Elkon R, and Agami R. A Pumilio-induced RNA structure switch in p27-3' UTR controls miR-221 and miR-222 accessibility. *Nat Cell*

650 *Biol.* 2010;12(10):1014-20.
651 14. Miles WO, Tschop K, Herr A, Ji JY, and Dyson NJ. Pumilio facilitates miRNA regulation of the
652 E2F3 oncogene. *Genes Dev.* 2012;26(4):356-68.
653 15. Temme C, Simonelig M, and Wahle E. Deadenylation of mRNA by the CCR4-NOT complex in
654 Drosophila: molecular and developmental aspects. *Front Genet.* 2014;5:143.
655 16. Van Etten J, Schagat TL, Hrit J, Weidmann CA, Brumbaugh J, Coon JJ, et al. Human Pumilio
656 proteins recruit multiple deadenylases to efficiently repress messenger RNAs. *J Biol Chem.*
657 2012;287(43):36370-83.
658 17. Weidmann CA, Raynard NA, Blewett NH, Van Etten J, and Goldstrohm AC. The RNA binding
659 domain of Pumilio antagonizes poly-adenosine binding protein and accelerates deadenylation. *RNA.*
660 2014;20(8):1298-319.
661 18. Goldstrohm AC, Hall TMT, and McKenney KM. Post-transcriptional Regulatory Functions of
662 Mammalian Pumilio Proteins. *Trends Genet.* 2018;34(12):972-90.
663 19. Bohn JA, Van Etten JL, Schagat TL, Bowman BM, McEachin RC, Freddolino PL, et al.
664 Identification of diverse target RNAs that are functionally regulated by human Pumilio proteins.
665 *Nucleic Acids Res.* 2018;46(1):362-86.
666 20. Uyhazi KE, Yang Y, Liu N, Qi H, Huang XA, Mak W, et al. Pumilio proteins utilize distinct
667 regulatory mechanisms to achieve complementary functions required for pluripotency and
668 embryogenesis. *Proc Natl Acad Sci U S A.* 2020;117(14):7851-62.
669 21. Marrero E, Rossi SG, Darr A, Tsoulfas P, and Rotundo RL. Translational regulation of
670 acetylcholinesterase by the RNA-binding protein Pumilio-2 at the neuromuscular synapse. *J Biol*
671 *Chem.* 2011;286(42):36492-9.
672 22. Muraro NI, Weston AJ, Gerber AP, Luschnig S, Moffat KG, and Baines RA. Pumilio binds para
673 mRNA and requires Nanos and Brat to regulate sodium current in Drosophila motoneurons. *J*
674 *Neurosci.* 2008;28(9):2099-109.
675 23. Raudvere U, Kolberg L, Kuzmin I, Arak T, Adler P, Peterson H, et al. g:Profiler: a web server for
676 functional enrichment analysis and conversions of gene lists (2019 update). *Nucleic Acids Res.*
677 2019;47(W1):W191-W8.
678 24. Zhang M, Chen D, Xia J, Han W, Cui X, Neuenkirchen N, et al. Post-transcriptional regulation of
679 mouse neurogenesis by Pumilio proteins. *Genes Dev.* 2017;31(13):1354-69.
680 25. Enwerem, III, Elrod ND, Chang CT, Lin A, Ji P, Bohn JA, et al. Human Pumilio proteins directly
681 bind the CCR4-NOT deadenylase complex to regulate the transcriptome. *RNA.* 2021;27(4):445-64.
682 26. Blewett NH, and Goldstrohm AC. A eukaryotic translation initiation factor 4E-binding protein

promotes mRNA decapping and is required for PUF repression. *Mol Cell Biol.* 2012;32(20):4181-94.
27. Wamsley B, Jaglin XH, Favuzzi E, Quattrocolo G, Nigro MJ, Yusuf N, et al. Rbfox1 Mediates Cell-type-Specific Splicing in Cortical Interneurons. *Neuron.* 2018;100(4):846-59 e7.
28. Gehman LT, Meera P, Stoilov P, Shiue L, O'Brien JE, Meisler MH, et al. The splicing regulator Rbfox2 is required for both cerebellar development and mature motor function. *Genes Dev.* 2012;26(5):445-60.
29. Kenny PJ, Kim M, Skariah G, Nielsen J, Lannom MC, and Ceman S. The FMRP-MOV10 complex: a translational regulatory switch modulated by G-Quadruplexes. *Nucleic Acids Res.* 2020;48(2):862-78.
30. Kenny PJ, Zhou H, Kim M, Skariah G, Khetani RS, Drnevich J, et al. MOV10 and FMRP regulate AGO2 association with microRNA recognition elements. *Cell Rep.* 2014;9(5):1729-41.
31. Singh K, Gaur P, and Prasad S. Fragile x mental retardation (Fmr-1) gene expression is down regulated in brain of mice during aging. *Mol Biol Rep.* 2007;34(3):173-81.
32. Singh K, and Prasad S. Differential expression of Fmr-1 mRNA and FMRP in female mice brain during aging. *Mol Biol Rep.* 2008;35(4):677-84.
33. Zamore PD, Williamson JR, and Lehmann R. The Pumilio protein binds RNA through a conserved domain that defines a new class of RNA-binding proteins. *RNA.* 1997;3(12):1421-33.
34. Agarwal V, Bell GW, Nam JW, and Bartel DP. Predicting effective microRNA target sites in mammalian mRNAs. *Elife.* 2015;4.
35. Gennarino VA, D'Angelo G, Dharmalingam G, Fernandez S, Russolillo G, Sanges R, et al. Identification of microRNA-regulated gene networks by expression analysis of target genes. *Genome Res.* 2012;22(6):1163-72.
36. Guan X, Chen S, Liu Y, Wang LL, Zhao Y, and Zong ZH. PUM1 promotes ovarian cancer proliferation, migration and invasion. *Biochem Biophys Res Commun.* 2018;497(1):313-8.
37. Dai H, Shen K, Yang Y, Su X, Luo Y, Jiang Y, et al. PUM1 knockdown prevents tumor progression by activating the PERK/eIF2/ATF4 signaling pathway in pancreatic adenocarcinoma cells. *Cell Death Dis.* 2019;10(8):595.
38. Lee S, Kopp F, Chang TC, Sataluri A, Chen B, Sivakumar S, et al. Noncoding RNA NORAD Regulates Genomic Stability by Sequestering PUMILIO Proteins. *Cell.* 2016;164(1-2):69-80.
39. Koopmans F, van Nierop P, Andres-Alonso M, Byrnes A, Cijsouw T, Coba MP, et al. SynGO: An Evidence-Based, Expert-Curated Knowledge Base for the Synapse. *Neuron.* 2019;103(2):217-34 e4.
40. Fu J, Peng L, Tao T, Chen Y, Li Z, and Li J. Regulatory roles of the miR-200 family in

716 neurodegenerative diseases. *Biomed Pharmacother.* 2019;119:109409.
717 41. Trumbach D, and Prakash N. The conserved miR-8/miR-200 microRNA family and their role in
718 invertebrate and vertebrate neurogenesis. *Cell Tissue Res.* 2015;359(1):161-77.
719 42. Keene JD. Biological clocks and the coordination theory of RNA operons and regulons. *Cold Spring*
720 *Harb Symp Quant Biol.* 2007;72:157-65.
721 43. Keene JD, and Lager PJ. Post-transcriptional operons and regulons co-ordinating gene expression.
722 *Chromosome Res.* 2005;13(3):327-37.
723 44. Blackinton JG, and Keene JD. Post-transcriptional RNA regulons affecting cell cycle and
724 proliferation. *Semin Cell Dev Biol.* 2014;34:44-54.
725 45. Maurin T, Lebrigand K, Castagnola S, Paquet A, Jarjat M, Popa A, et al. HITS-CLIP in various
726 brain areas reveals new targets and new modalities of RNA binding by fragile X mental retardation
727 protein. *Nucleic Acids Res.* 2018;46(12):6344-55.
728 46. Chi SW, Zang JB, Mele A, and Darnell RB. Argonaute HITS-CLIP decodes microRNA-mRNA
729 interaction maps. *Nature.* 2009;460(7254):479-86.
730 47. Weyn-Vanhentenryck SM, Mele A, Yan Q, Sun S, Farny N, Zhang Z, et al. HITS-CLIP and
731 integrative modeling define the Rbfox splicing-regulatory network linked to brain development and
732 autism. *Cell Rep.* 2014;6(6):1139-52.
733 48. Subramanian A, Tamayo P, Mootha VK, Mukherjee S, Ebert BL, Gillette MA, et al. Gene set
734 enrichment analysis: a knowledge-based approach for interpreting genome-wide expression profiles.
735 *Proc Natl Acad Sci U S A.* 2005;102(43):15545-50.
736 49. Charizanis K, Lee KY, Batra R, Goodwin M, Zhang C, Yuan Y, et al. Muscleblind-like 2-mediated
737 alternative splicing in the developing brain and dysregulation in myotonic dystrophy. *Neuron.*
738 2012;75(3):437-50.
739 50. Zhang C, Frias MA, Mele A, Ruggiu M, Eom T, Marney CB, et al. Integrative modeling defines the
740 Nova splicing-regulatory network and its combinatorial controls. *Science.* 2010;329(5990):439-43.
741 51. Preitner N, Quan J, Nowakowski DW, Hancock ML, Shi J, Tcherkezian J, et al. APC is an RNA-
742 binding protein, and its interactome provides a link to neural development and microtubule
743 assembly. *Cell.* 2014;158(2):368-82.
744 52. Licatalosi DD, Yano M, Fak JJ, Mele A, Grabinski SE, Zhang C, et al. Ptbp2 represses adult-specific
745 splicing to regulate the generation of neuronal precursors in the embryonic brain. *Genes Dev.*
746 2012;26(14):1626-42.
747 53. Chen D, Zheng W, Lin A, Uyhazi K, Zhao H, and Lin H. Pumilio 1 suppresses multiple activators of
748 p53 to safeguard spermatogenesis. *Curr Biol.* 2012;22(5):420-5.

54. Bonnemason-Carrere P, Morice-Picard F, Pennamen P, Arveiler B, Fergelot P, Goizet C, et al. PADDAS syndrome associated with hair dysplasia caused by a de novo missense variant of PUM1. *Am J Med Genet A.* 2019;179(6):1030-3.
55. Imaizumi T, Mogami Y, Okamoto N, Yamamoto-Shimojima K, and Yamamoto T. De novo 1p35.2 microdeletion including PUM1 identified in a patient with sporadic West syndrome. *Congenit Anom (Kyoto).* 2019;59(6):193-4.
56. Lai KL, Liao YC, Tsai PC, Hsiao CT, Soong BW, and Lee YC. Investigating PUM1 mutations in a Taiwanese cohort with cerebellar ataxia. *Parkinsonism Relat Disord.* 2019;66:220-3.
57. Tan Q, and Zoghbi HY. Mouse models as a tool for discovering new neurological diseases. *Neurobiol Learn Mem.* 2019;165:106902.
58. Kim K, Hessl D, Randol JL, Espinal GM, Schneider A, Protic D, et al. Association between IQ and FMR1 protein (FMRP) across the spectrum of CGG repeat expansions. *PLoS One.* 2019;14(12):e0226811.
59. Chartier-Harlin MC, Kachergus J, Roumier C, Mouroux V, Douay X, Lincoln S, et al. Alpha-synuclein locus duplication as a cause of familial Parkinson's disease. *Lancet.* 2004;364(9440):1167-9.
60. Rovelet-Lecrux A, Hannequin D, Raux G, Le Meur N, Laquerriere A, Vital A, et al. APP locus duplication causes autosomal dominant early-onset Alzheimer disease with cerebral amyloid angiopathy. *Nat Genet.* 2006;38(1):24-6.
61. Takeguchi R, Takahashi S, Kuroda M, Tanaka R, Suzuki N, Tomonoh Y, et al. MeCP2_e2 partially compensates for lack of MeCP2_e1: A male case of Rett syndrome. *Mol Genet Genomic Med.* 2020;8(2):e1088.
62. Orr HT, and Zoghbi HY. Trinucleotide repeat disorders. *Annu Rev Neurosci.* 2007;30:575-621.
63. Bah MG, Rodriguez D, Cazeneuve C, Mochel F, Devos D, Suppiej A, et al. Deciphering the natural history of SCA7 in children. *Eur J Neurol.* 2020;27(11):2267-76.
64. Tereshchenko A, Magnotta V, Epping E, Mathews K, Espe-Pfeifer P, Martin E, et al. Brain structure in juvenile-onset Huntington disease. *Neurology.* 2019;92(17):e1939-e47.
65. Genetic Modifiers of Huntington's Disease C. Identification of Genetic Factors that Modify Clinical Onset of Huntington's Disease. *Cell.* 2015;162(3):516-26.
66. Kacher R, Lejeune FX, Noel S, Cazeneuve C, Brice A, Humbert S, et al. Propensity for somatic expansion increases over the course of life in Huntington disease. *Elife.* 2021;10.
67. Salcedo-Arellano MJ, Dufour B, McLennan Y, Martinez-Cerdeno V, and Hagerman R. Fragile X syndrome and associated disorders: Clinical aspects and pathology. *Neurobiol Dis.*

2020;136:104740.
68. Shah S, Molinaro G, Liu B, Wang R, Huber KM, and Richter JD. FMRP Control of Ribosome Translocation Promotes Chromatin Modifications and Alternative Splicing of Neuronal Genes Linked to Autism. *Cell Rep.* 2020;30(13):4459-72 e6.
69. Conboy JG. Developmental regulation of RNA processing by Rbfox proteins. *Wiley Interdiscip Rev RNA.* 2017;8(2).
70. Smidak R, Sialana FJ, Kristofova M, Stojanovic T, Rajcic D, Malikovic J, et al. Reduced Levels of the Synaptic Functional Regulator FMRP in Dentate Gyrus of the Aging Sprague-Dawley Rat. *Front Aging Neurosci.* 2017;9:384.
71. Pfaffl MW. A new mathematical model for relative quantification in real-time RT-PCR. *Nucleic Acids Res.* 2001;29(9):e45.

Supplemental figures

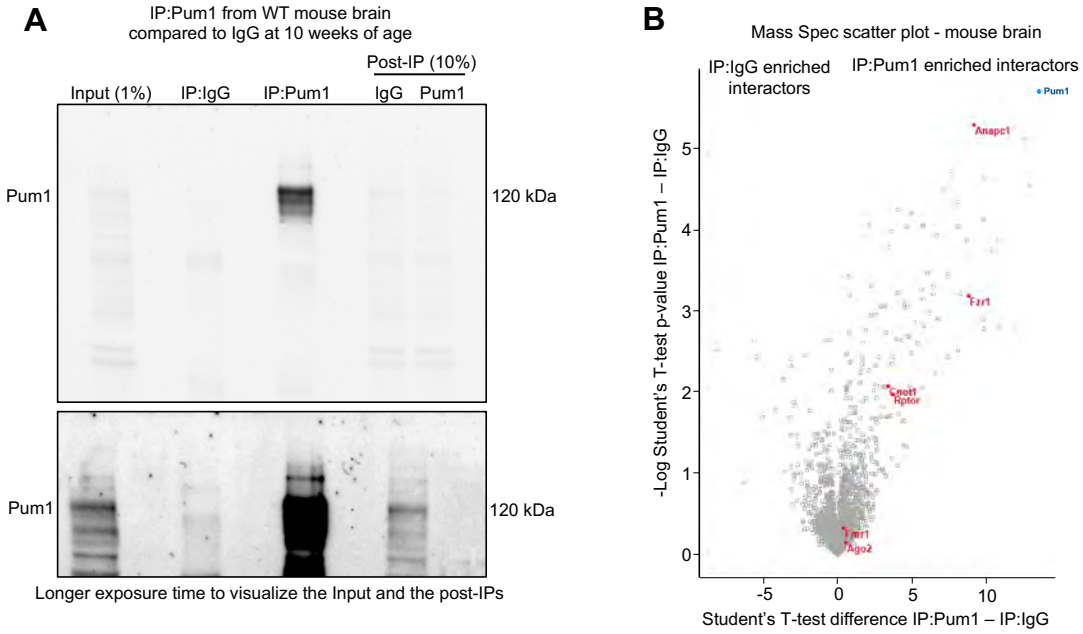

Supplemental Figure 1. Pumilio1 antibody efficiency. (**A**) Pre-IP, IP, and post-IP against Pum1 and IgG from wild-type mouse brain. Even at very long exposure, the post-IP Pum1 lane has no residual band at 120 kDa even though 10 times more protein is loaded than Input. This demonstrates the high efficiency of the Pum1 antibody, which makes it suitable for IP mass spec. The numbers on the right show molecular weight in kilodaltons (kDa). (**B**) Volcano plot analysis showing all the proteins pulled down by IP against IgG and Pum1 from mouse brain.

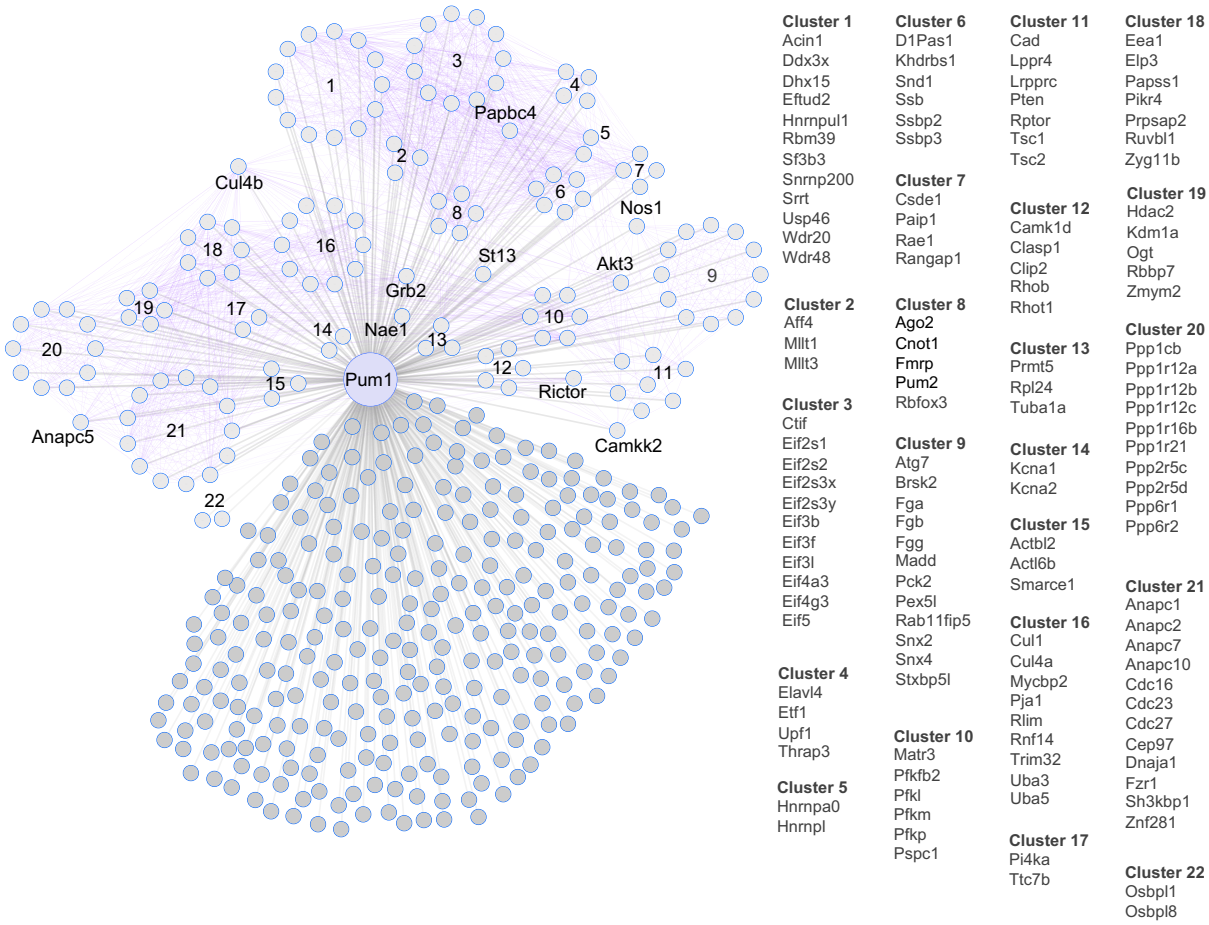

Supplemental Figure 2. A brain-specific Pum1 interactome. Network of putative Pum1 interactors in 10-week-old mouse brain (circles connected to Pum1 by gray lines). Interactions between interactors (purple lines) were inferred by g:GOSt from Corum and the Human Protein Atlas (see Methods). The proteins in each of the 22 clusters are listed to the right. We combined and homogenized whole brains from two 10-week-old wild-type mice per sample (1 female and 1 male), aliquoting half of each sample for IP against either Pum1 or IgG, then performed six biological replicates (six samples, 12 mice total) for each mass spec experiment against IP-Pum1 and IP-IgG. All putative Pum1 interactors are listed in Supplemental Table 1.

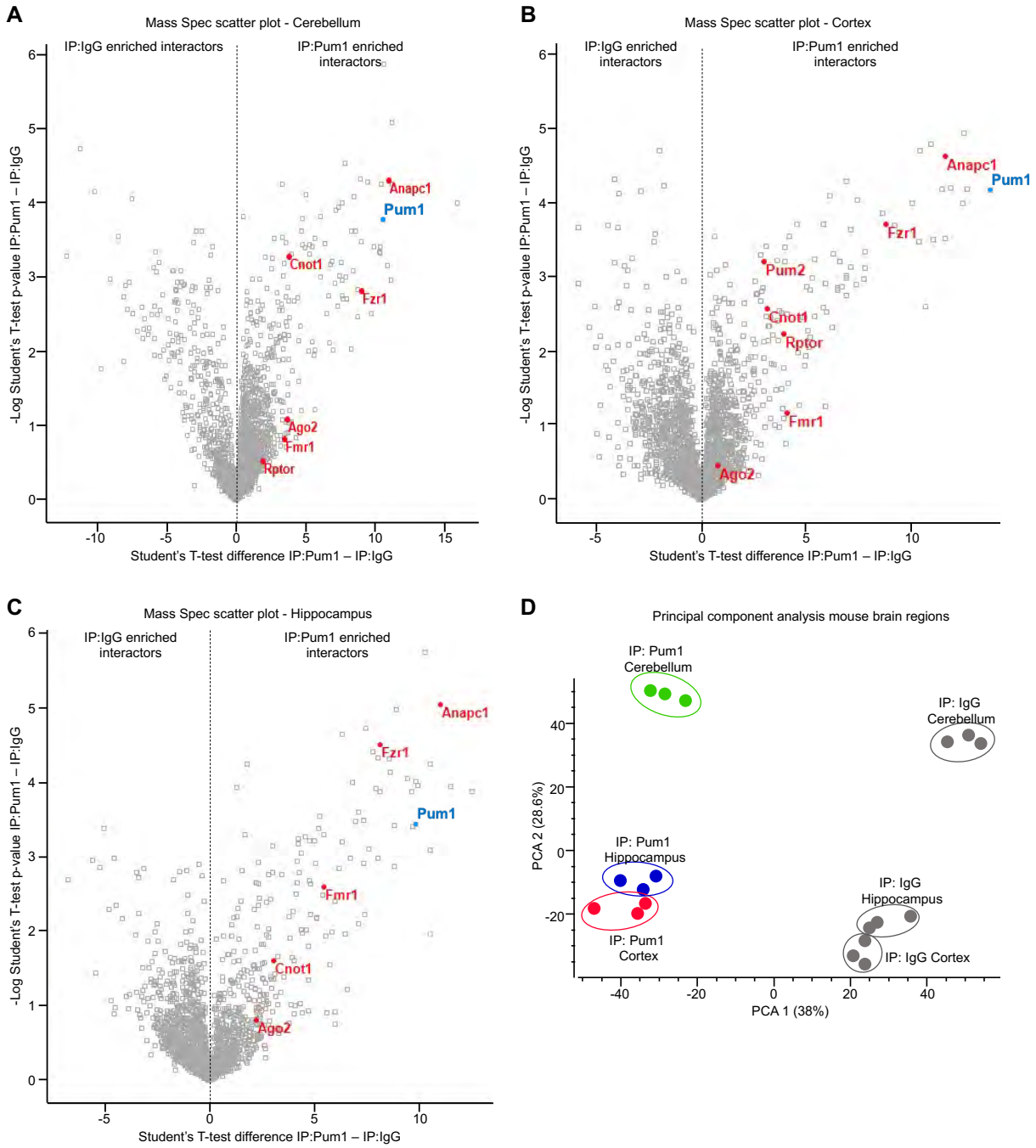

Supplemental Figure 3. Volcano plot and PCA analyses of IP:Pum1 followed by mass spectrometry in cerebellum, hippocampus, and cortex. (**A-C**) Volcano plots show all the proteins pulled down by IP against IgG and Pum1 from (**A**) cerebellum, (**B**) cortex, and (**C**) hippocampus at 10 weeks of age. (**D**) Principal component analysis (PCA) of IP-Pum1 followed by mass spectrometry (MS) in cortex, hippocampus, and cerebellum from WT mice. IP against IgG was used as a negative control. Each dot represents a total of 3 samples processed by MS for each brain region. All putative Pum1 interactors are listed in Supplemental Table 1.

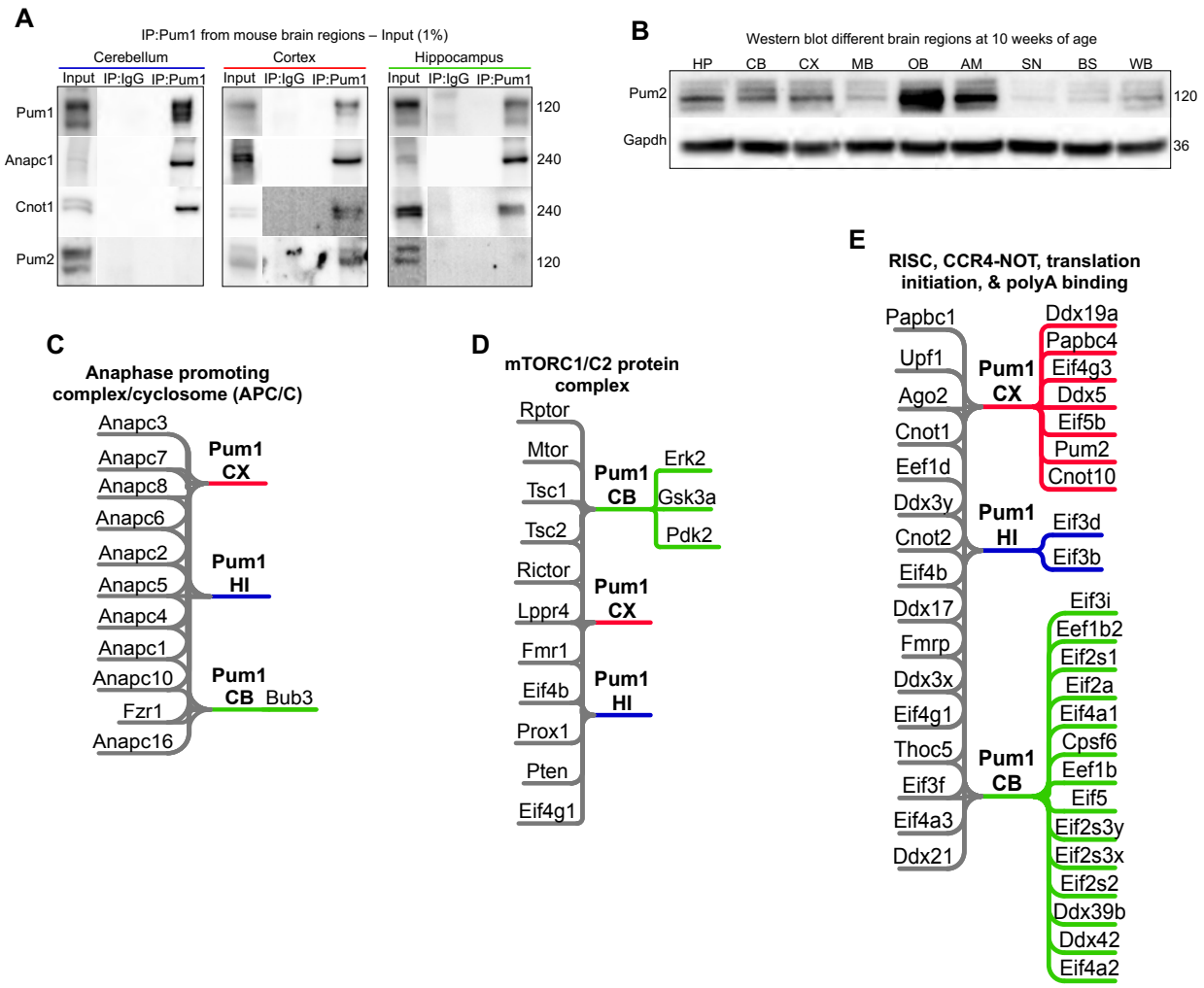

Supplemental Figure 4. Pum1 interactors can differ by brain region. (**A**) Immunoblot for Pum1 (positive control), Anapc1, Cnot1 and Pum2. While Cnot1 and Anapc1 can be pulled down from all three brain regions, Pum2 can only be pulled down from cortex. All experiments performed in triplicate. Cerebellar and cortical tissues: n=8 wild-type mice (4 male and 4 female), for a total of 24 mice. Hippocampus: n=10 wild-type mice (5 female and 5 male), for a total of 30 mice. All mice were 10 weeks of age. IP against IgG was used as a negative control. Molecular protein weights are expressed in kilodaltons (kDa). (**B**) Western blot analysis at 10 weeks of age to evaluate Pum2 expression levels in eight different brain regions as well as whole brain. Pum2 is highly expressed in olfactory bulbs and amygdala, and expressed at similar levels in hippocampus, cerebellum, and cortex. HP: hippocampus; CB: cerebellum; CX: cortex; MB: midbrain; OB: olfactory bulbs; AM: amygdala; SN: substantia nigra pars compacta; BS: brain stem; WB: whole brain. All the experiments were repeated at least three times. (**C**-**E**) The three most enriched protein complexes among the Pum1 interactors for each brain region are shown in (**C**) for the anaphase promoting complex/cyclosome (APC/C); (**D**) for the mTOR pathway; (**E**) for RNA-silencing (RISC), CCR4-NOT, translation initiation and polyA binding. Edge colors (**C**-**E**) represent a specific brain region: red for cortex, green for cerebellum, blue for hippocampus, and gray for proteins in common between two or more brain regions.

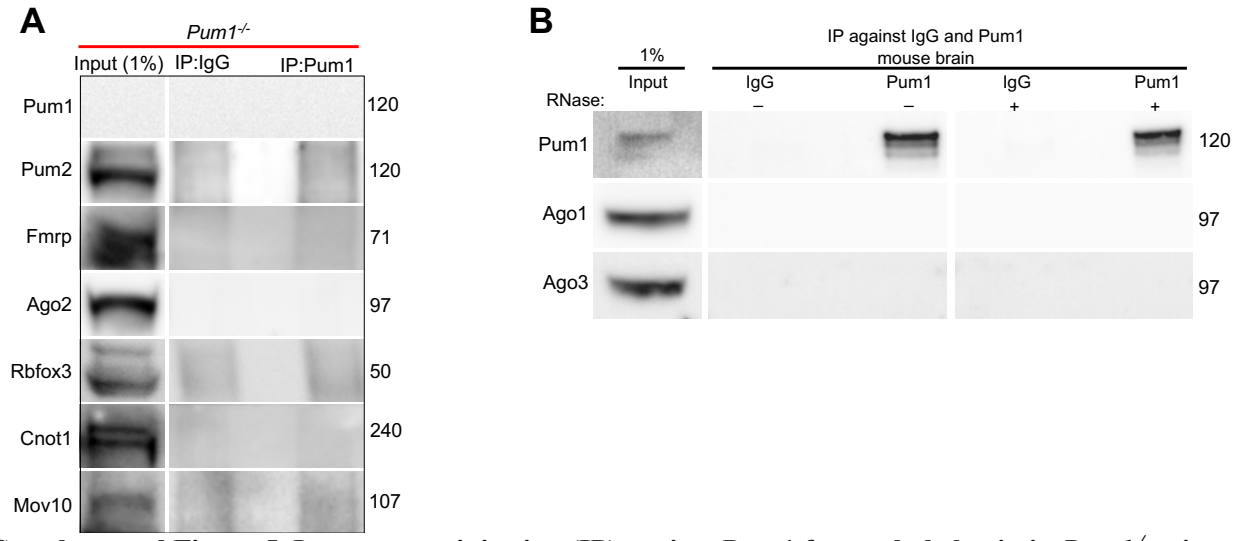

Supplemental Figure 5. Immunoprecipitation (IP) against Pum1 from whole brain in *Pum1*$^{-/-}$ mice. **(A)** IP against Pum1 in *Pum1*$^{-/-}$ mouse demonstrates the complete absence of Pum1 and thus the specificity of the anti-Pum1 antibody. IP against IgG was used as a negative control, and Input (1% from the initial protein lysate) as a loading control. (**B**) IP against Pum1 (with or without RNase treatment) shows no interaction with Ago1 or Ago3 in the mouse brain. These lanes are from the same experiment shown in Figure 2A, so the Pum1 row is precisely the same. Molecular weights at the right are in kilodaltons (kDa). All the experiments were repeated at least three times. IP against IgG was used as a negative control, and Input (1% from the initial protein lysate) as a loading control. Equal numbers of male and female mice were sacrificed at 10 weeks of age.

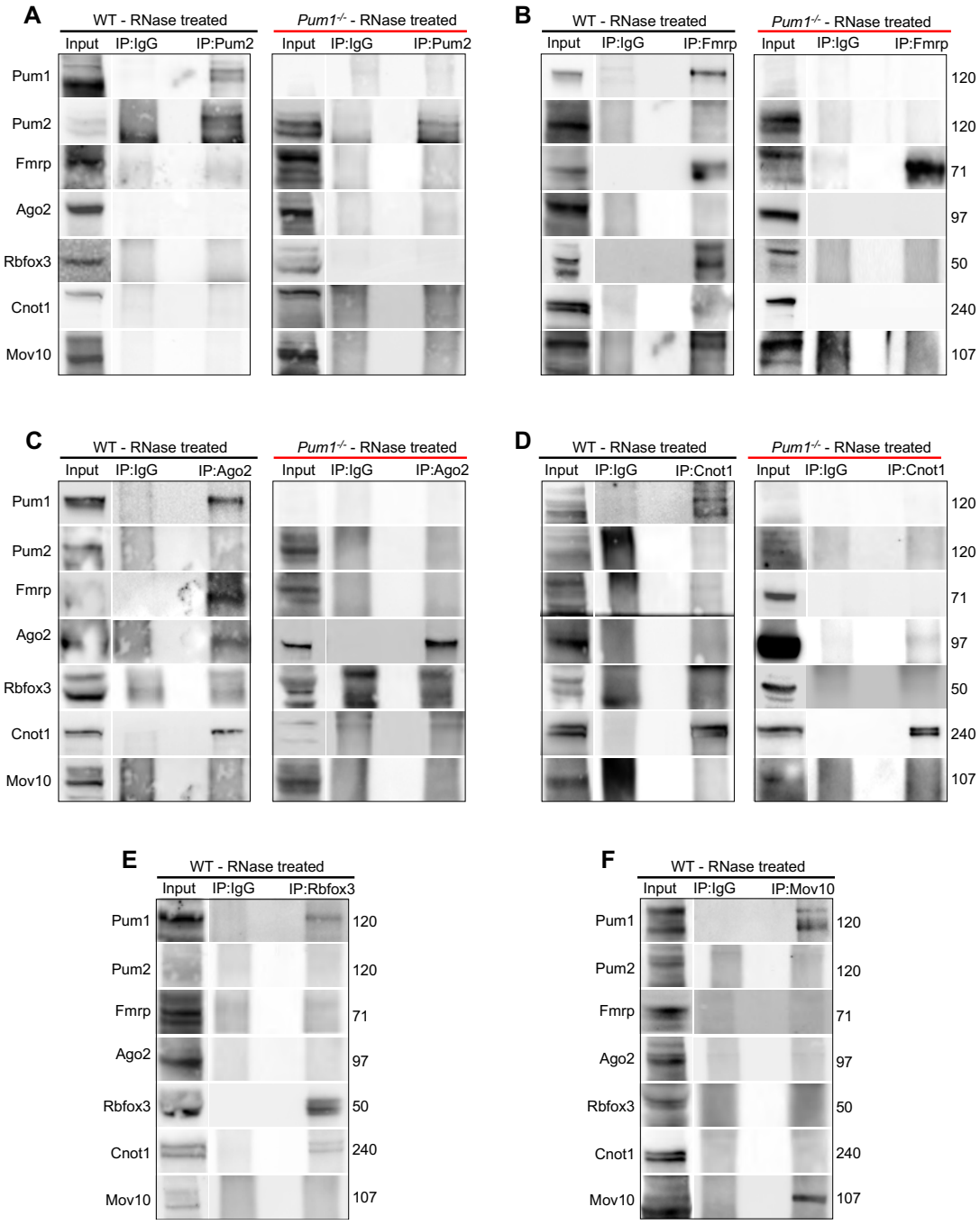

Supplemental Figure 6. Immunoprecipitation (IP) against Pum1 interactors from whole brain in wild-type and *Pum1*$^{-/-}$ mice with RNase treatment. (**A**-**F**) Representative western blots of the proteins pulled down by (**A**) Pum2, (**B**) Fmrp, (**C**) Ago2, (**D**) Cnot1, (**E**) Rbfox3, and (**F**) Mov10 from wild-type (WT, *left panel*) and *Pum1*$^{-/-}$ (*right panel*) mouse brain. IP against IgG was used as a negative control, and Input (1% from the initial protein lysate) as a loading control. Molecular weights at the right are in kilodaltons (kDa). All the experiments were repeated at least three times. IP against IgG was used as a negative control, and Input (1% from the initial protein lysate) as a loading control. Equal numbers of male and female mice were sacrificed at 10 weeks of age.

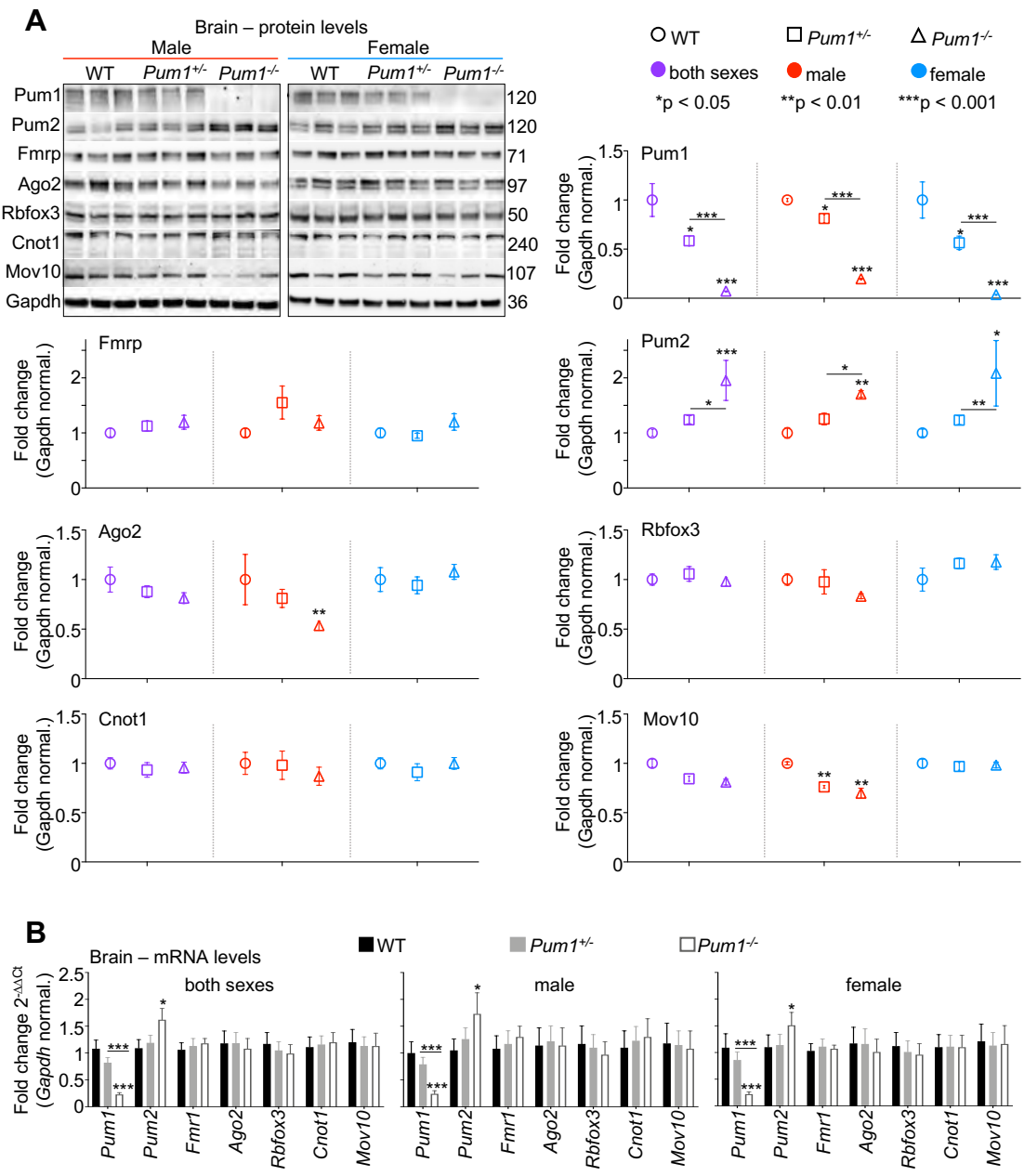

Supplemental Figure 7. Protein and mRNA quantification from WT, *Pum1*$^{+/-}$ and *Pum1*$^{-/-}$ mouse brains. (**A**) Representative western blot with relative quantifications of Pum1, Pum2, Fmrp, Ago2, Rbfox3, Cnot1, and Mov10 from whole brains of WT, *Pum1*$^{+/-}$ and *Pum1*$^{-/-}$ mice. All data were normalized to Gapdh protein levels. The numbers on the right are the respective molecular weights expressed in kilodaltons (kDa). (**B**) mRNA level quantification by qPCR of *Pum1*, *Pum2*, *Fmrp*, *Ago2*, *Rbfox3*, *Cnot1*, and *Mov10* from whole brains of WT, *Pum1*$^{+/-}$ and *Pum1*$^{-/-}$ mice. Again, all data were normalized to *Gapdh* mRNA levels. All the experiments were conducted with equal number of male (at least 6 per genotype) and female (at least 6 per genotype) mice at 10 weeks of age, for a total of at least 12 mice per genotype (data represent mean ± SEM). The *p* values were calculated by the Student's t test. **p* < 0.05, ***p* < 0.01, ****p* < 0.001.

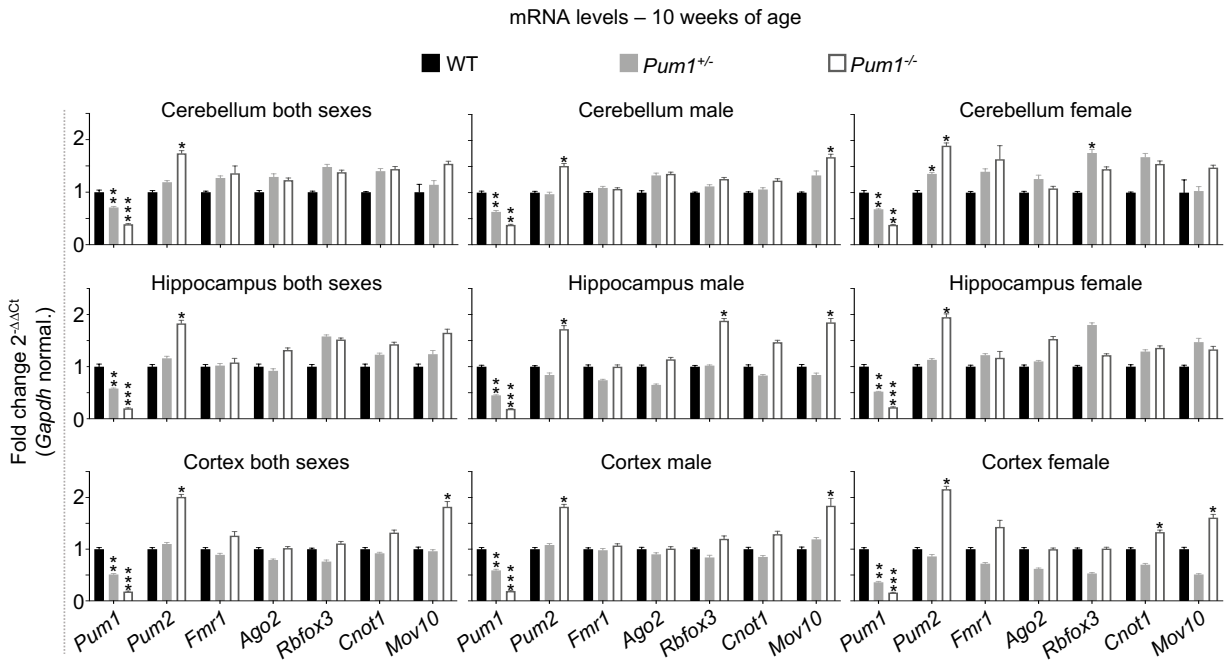

Supplemental Figure 8. mRNA quantification of Pum1 interactors by brain region and sex in WT, *Pum1*$^{+/-}$ and *Pum1*$^{-/-}$ mice. mRNA levels in cerebellum, hippocampus, and cortex in male and female for all the validated Pum1 interactors. The same number of mice were used here as in **Figure 4A-C** for a total of at least 12 mice per genotype and sex at 10 weeks of age. All data were normalized to *Gapdh* mRNA levels. All the experiments were performed at least six times (data represent mean ± SEM). The *p* values were calculated by the Student's t test. *$p < 0.05$, **$p < 0.01$, ***$p < 0.001$.

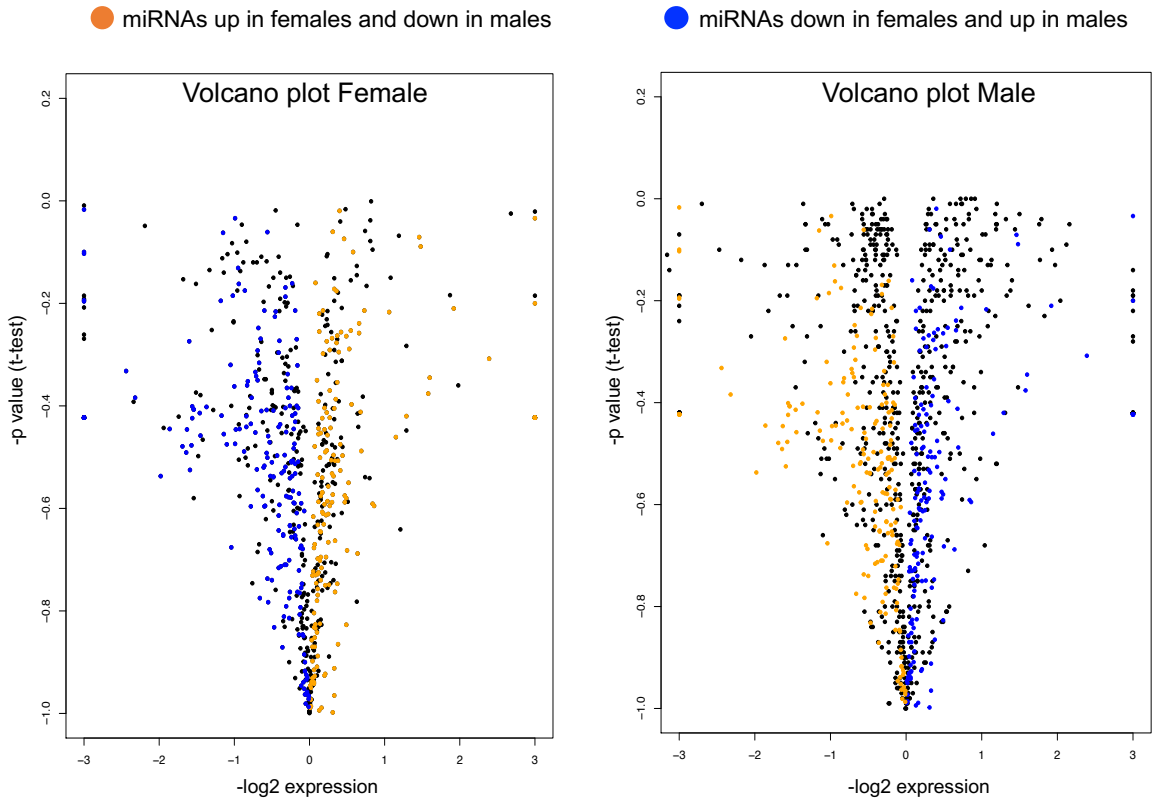

Supplemental Figure 9. Volcano plots representing all the miRNAs sequenced by miRNAseq in male and female. Volcano plots show the expression profile for all the miRNAs in male and female *Pum1*$^{-/-}$ mice compared to WT at 10 weeks of age. The orange dots represent the miRNAs upregulated in female and downregulated in males; the blue dots represent the miRNAs downregulated in female and upregulated in males. miRNAseq was performed in triplicate (see Methods).

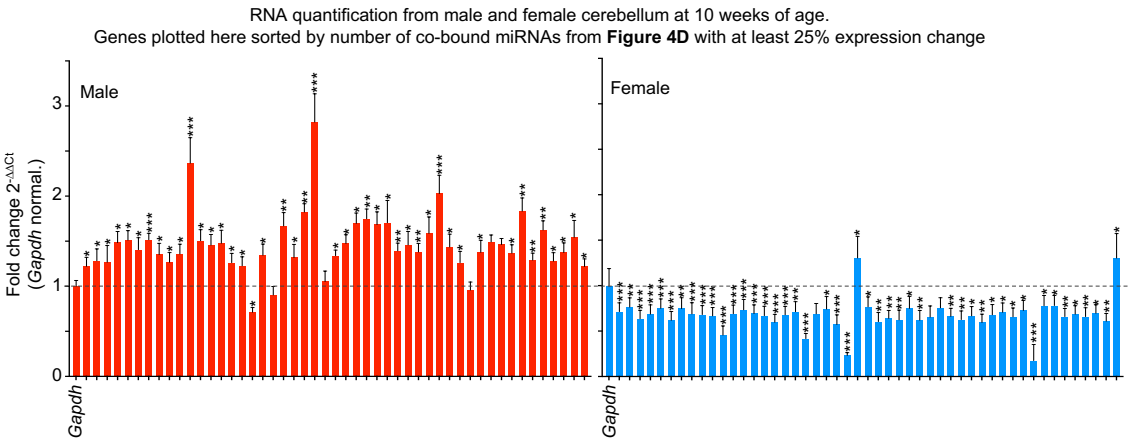

Table showing the order of gene represented in the figure above starting from *Gapdh* as represented in Figure 4E

Position in the graph	Gene	Male	Female	Error_Male	Error_Female	Co-bound miRNAs
1	*Gapdh*	1.000	1.000	0.065	0.188	11
2	*Aak1*	1.222	0.714	0.099	0.096	11
3	*Plekhm3*	1.283	0.764	0.132	0.102	11
4	*Zbtb20*	1.268	0.636	0.185	0.093	10
5	*Ago3*	1.485	0.686	0.122	0.102	10
6	*Dgkh*	1.511	0.751	0.106	0.103	10
7	*Fto*	1.407	0.618	0.132	0.097	10
8	*Grin2b*	1.517	0.749	0.071	0.117	10
9	*Lpp*	1.353	0.689	0.124	0.123	10
10	*Stx17*	1.266	0.682	0.108	0.098	10
11	*Acvr2b*	1.359	0.668	0.108	0.092	9
12	*Ap5m1*	2.366	0.456	0.282	0.101	9
13	*Chl1*	1.506	0.691	0.121	0.094	9
14	*Gpr161*	1.457	0.735	0.118	0.113	9
15	*Kcnn3*	1.477	0.694	0.145	0.094	9
16	*Klf7*	1.262	0.670	0.103	0.103	9
17	*Nfat5*	1.228	0.598	0.099	0.086	9
18	*Plxna4*	0.712	0.680	0.051	0.092	9
19	*Slc1a2*	1.344	0.713	0.125	0.111	9
20	*Slc8a1*	0.904	0.417	0.094	0.056	9
21	*Ston2*	1.669	0.690	0.148	0.114	9
22	*Tsc22d2*	1.319	0.743	0.146	0.137	9
23	*Xkr4*	1.823	0.573	0.093	0.105	9
24	*A1cf*	2.821	0.232	0.314	0.031	8
25	*Aff4*	1.053	1.304	0.116	0.238	8
26	*Clstn2*	1.340	0.768	0.062	0.109	8
27	*Cnnm2*	1.475	0.605	0.097	0.099	8
28	*Csnk1a1*	1.698	0.641	0.115	0.087	8
29	*Ctdspl2*	1.749	0.624	0.108	0.108	8
30	*Dcaf7*	1.685	0.750	0.141	0.132	8
31	*Fmnl3*	1.705	0.620	0.246	0.106	8
32	*Frmd4a*	1.394	0.654	0.085	0.123	8
33	*Grin2a*	1.459	0.755	0.148	0.112	8
34	*Hipk2*	1.381	0.662	0.094	0.088	8
35	*Kif26b*	1.588	0.627	0.181	0.094	8
36	*Klf12*	2.030	0.668	0.202	0.101	8
37	*Lmln*	1.435	0.595	0.143	0.091	8
38	*Lrrc40*	1.262	0.679	0.126	0.113	8
39	*Myo5a*	0.958	0.707	0.089	0.102	8
40	*Nav2*	1.377	0.658	0.135	0.097	8
41	*Psd3*	1.493	0.728	0.076	0.110	8
42	*Ptbp2*	1.463	0.177	0.068	0.177	8
43	*Rimkla*	1.368	0.779	0.092	0.112	8
44	*Snx30*	1.833	0.781	0.147	0.112	8
45	*Taok1*	1.290	0.660	0.078	0.088	8
46	*Zbtb10*	1.624	0.686	0.102	0.092	8
47	*Apbb2*	1.278	0.660	0.094	0.097	8
48	*Acap2*	1.374	0.697	0.107	0.093	8
49	*Acer2*	1.544	0.610	0.187	0.083	8
50	*Aebp2*	1.219	1.904	0.085	0.269	8

Supplemental Figure 10. mRNA quantification of the 49 targets co-bound by at least eight dysregulated miRNAs in mouse cerebellum. qPCR in cerebellum of male (*left*, red) and female (*right*, blue) mice at 10 weeks of age for the 49 targets co-bound by at least eight dysregulated miRNAs (with minimum 25% change in expression) from Figure 4E and Supplemental Table 4. All the experiments were performed in triplicate for both male and female (data represent mean ± SEM). The *p* values were calculated by two-tailed Student's t test. *$p < 0.05$, **$p < 0.01$, ***$p < 0.001$.

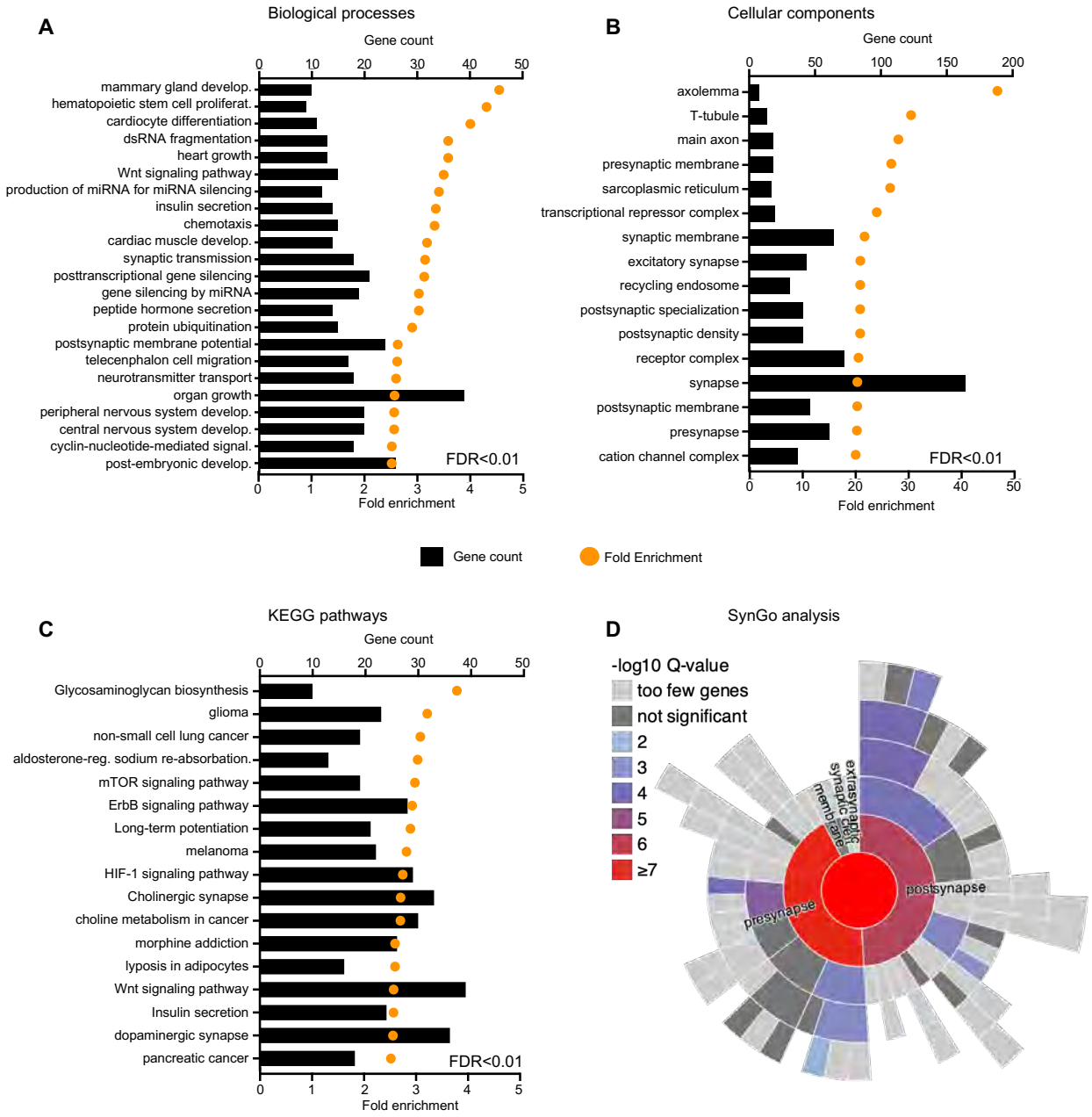

Supplemental Figure 11. Gene ontology analysis for all targets predicted by CoMeTa and TargetScan that are co-bound by at least four miRNAs. (**A-C**) David Gene Ontology representing the enriched (**A**) biological processes, (**B**) cellular components, and (**C**) KEGG pathways for all the targets co-bound by at least four miRNAs. For this analysis we set FDR<0.01 and a fold-enrichment >2. (**D**) Synaptic Gene Ontology (SynGO) predicts that 117 targets are are presynaptic and 124 are postsynaptic with a log10Q value≥5.

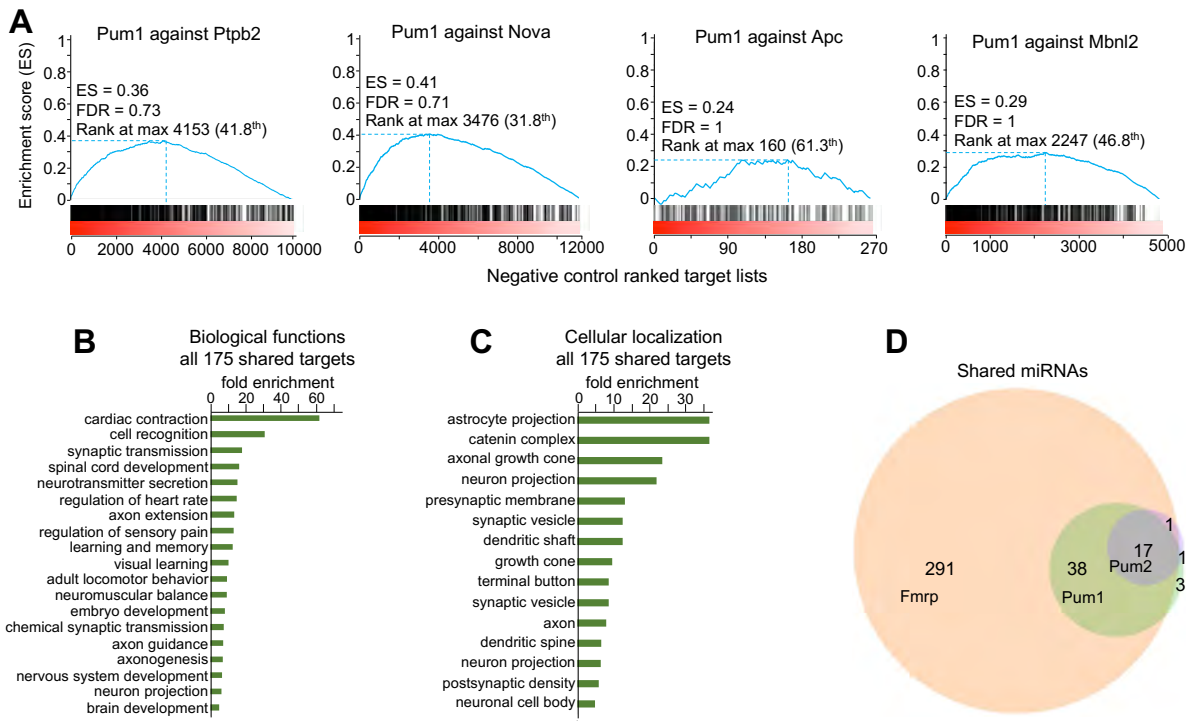

Supplemental Figure 12. GSEA and Gene Ontology data pertaining to Figure 5. (**A**) Gene Set Enrichment Analysis (GSEA) of Pum1 HITS-CLIP data plotted against HITS-CLIP data from the negative controls (RBPs that did not show up in the Pum1 interactome: Ptpb2, Nova, Apc, and Mbnl2) reveals no significant enrichment. (**B**-**C**) Gene ontology analysis of the HITS-CLIP targets shared between Pum1, Pum2, Fmrp, Ago2, and Rbfox3 reveals enrichment for certain (**B**) biological functions and (**C**) cellular localization. Only categories with FDR<0.05 and fold enrichment > 5 were plotted in **B** and **C**. (**D**) Venn diagram of miRNAs identified by Pum1 and Pum2 shows almost 100% overlap with the miRNAs pulled down by Fmrp HITS-CLIP. For full list of shared miRNAs see Supplemental Table 6. For all GSEA analyses the False Discovery Rate (FDR) was provided by GSEA, ***FDR < 0.01. ES=Enrichment score (blue line).

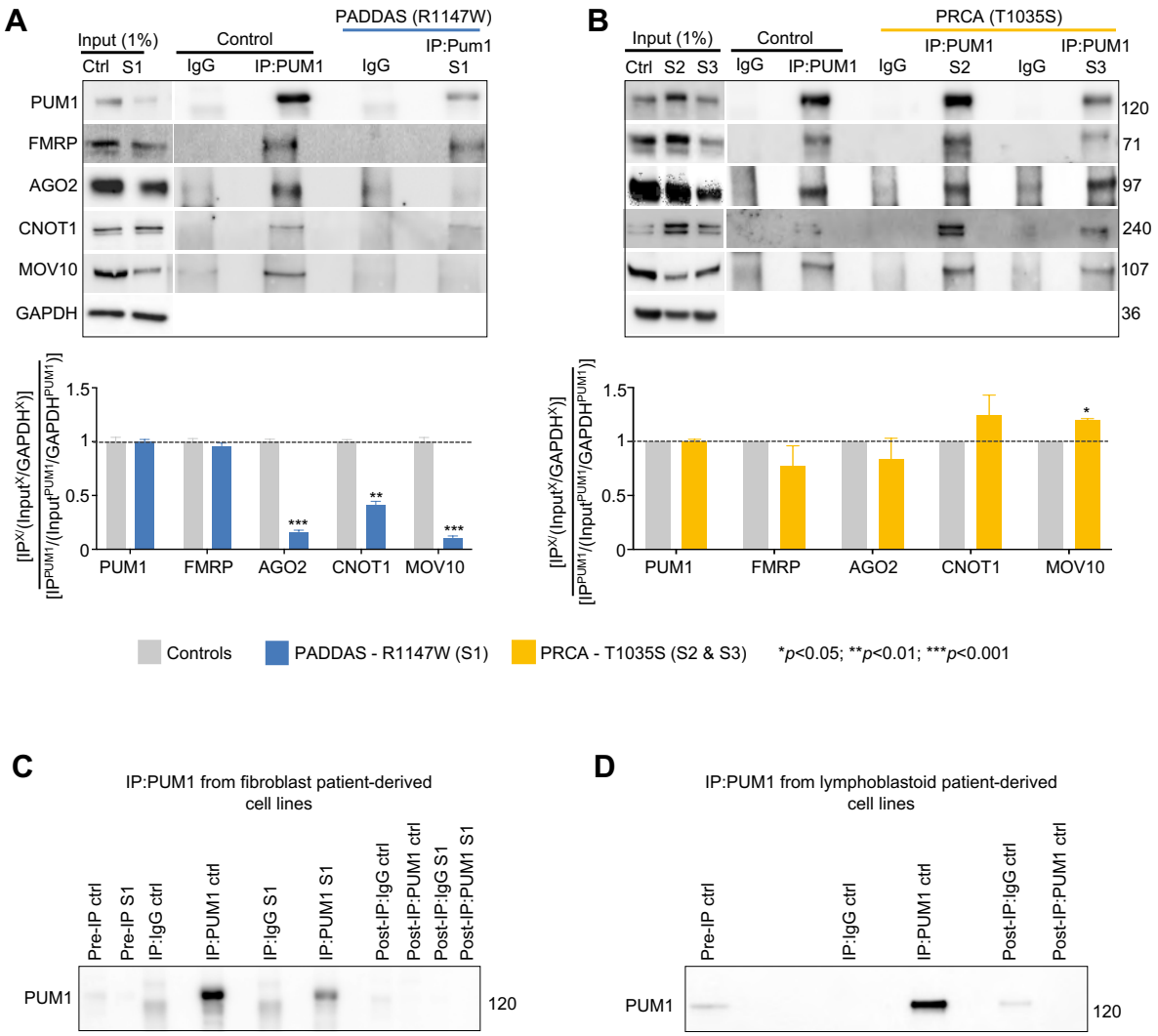

Supplemental Figure 13. PUM1 validation experiments in patient-derived cells. (**A**) IP against PUM1 from PADDAS (R1147W; Subject 1 or S1) patient-derived fibroblasts confirms the interactions between PUM1 (used here as a positive control), and PUM2, FMRP, AGO2, CNOT1, and MOV10. *Bottom panel*: protein quantification shows loss of interaction between PUM1-R1147W and AGO2, CNOT1 and MOV10 compared to three age- and sex- matched control fibroblasts. Input (1%) was used as a loading control and IP against IgG was used as a negative control. (**B**) IP against PUM1 from two PRCA (T1035S) patient-derived lymphoblastoid cell lines (S2 and S3) confirm the interaction between PUM1 (used here as positive control), and PUM2, FMRP, AGO2, CNOT1, and MOV10. *Bottom panel*: protein quantification shows a slight decrease in interactions with FMRP and AGO2, and a slight increase with CNOT1 and MOV10, compared to age- and sex- matched lymphoblastoid controls. Input (1%) was used as a loading control and IP against IgG was used as a negative control. In **A** and **B**, the amount of protein pulled down compared to IP-PUM1 was quantified as follows: $[IP^{X}/(Input^{X}/GAPDH^{X})]/[IP^{PUM1}/(Input^{PUM1}/GAPDH^{PUM1})]$, where X is the protein of interest. All the IPs were repeated at least three times. Data represent mean ± SEM. P values were calculated by two-tailed Student's t test. *$p < 0.05$, **$p < 0.01$, ***$p < 0.001$. (**C**-**D**) Pre-IP, IP, and post-IP against PUM1 and IgG from (**C**) PADDAS fibroblasts and (**D**) PRCA lymphoblastoid cells. In both cell lines we were able to pull down 100% of PUM1. Pre-IP represents 1% from the initial protein lysate as a loading control, while 10% of the protein lysate was loaded as post-IP. Molecular weights provided at right in kilodaltons (kDa).

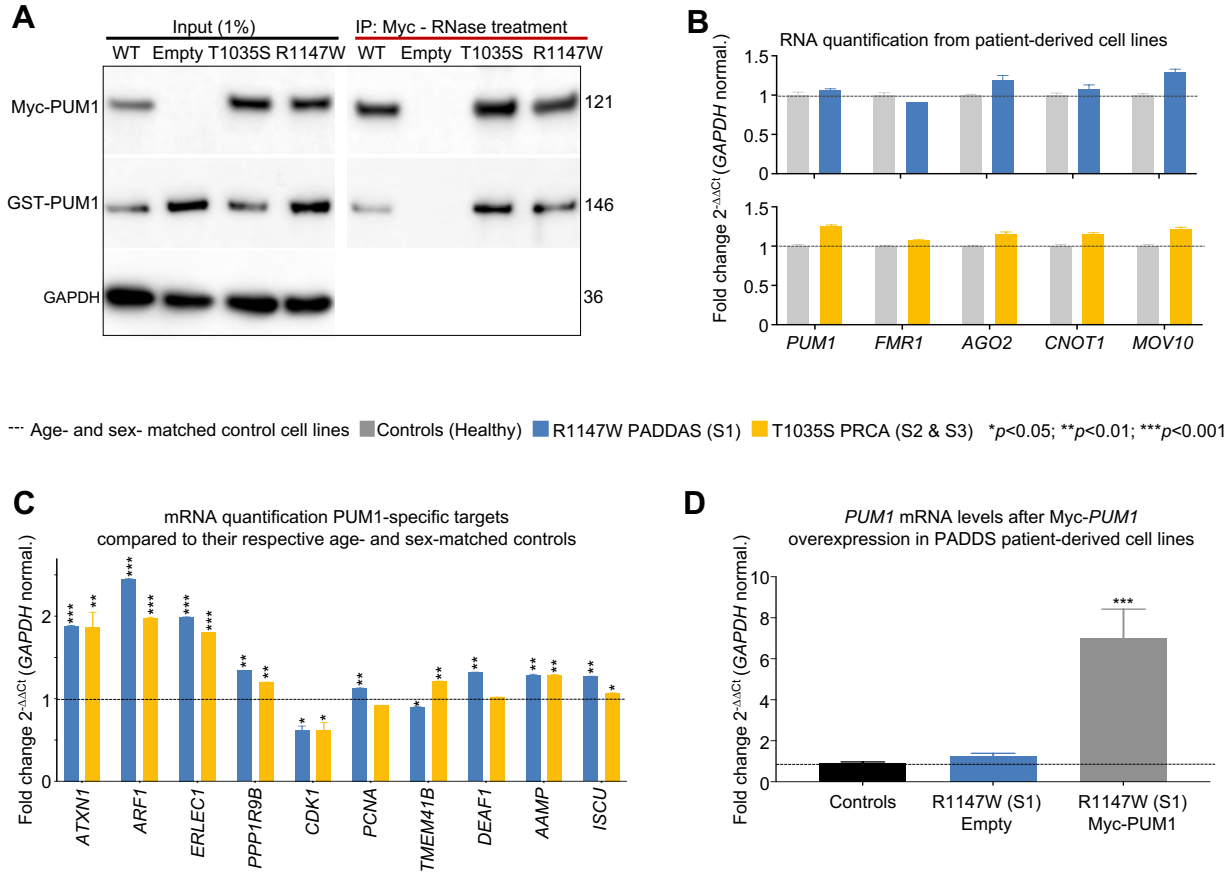

Supplemental Figure 14. PUM1 dimerization with RNase treatment, quantification of PUM1 interactor mRNA and PUM1-specific targets in patient-derived cell lines. (**A**) Representative western blots of IP with RNase treatment against Myc-PUM1-WT, Myc-PUM1-T1035S (PRCA), and Myc-PUM1-R1147W (PADDAS) followed by immunoblotting to test binding between PUM1 proteins without the RNA. The numbers on the right are the respective molecular weights expressed in kilodaltons (kDa). (**B**) mRNA quantification for all of the immunoblotted proteins in Figure 6E in PADDAS and PRCA patient-derived cell lines compared to their respective age-, sex-, and cell-type-matched controls. (**C**) qPCR analysis of validated PUM1-specific targets from PADDAS patient-derived fibroblasts (blue bars) compared to three age- and sex-matched fibroblast control cell lines, and PRCA patient-derived lymphoblastoid cell lines (orange bars) compared to three age- and sex-matched lymphoblastoid control cell lines. Only genes expressed in both fibroblasts and lymphoblasts are represented here, for a total of 10 genes. (**D**) mRNA quantification of PUM1 from PADDAS patient-derived fibroblasts transfected with empty and Myc-PUM1-WT vectors, compared to three age- and sex-matched fibroblast control cell lines. For **B**, **C**, and **D** all data were normalized to *GAPDH* mRNA levels and experiments performed at least three times. Data represent mean ± SEM. P values were calculated by two-tailed Student's t test. *$p < 0.05$, **$p < 0.01$, ***$p < 0.001$.

Supplemental Methods

HEK293T cell culture and maintenance

Human embryonic kidney immortalized 293T (HEK293T) cells were grown in DMEM (GenDepot, #CM002-320) supplemented with 10% of heat-inactivated fetal bovine serum (FBS [GenDepot, #F0901-050) and 1% penicillin/streptomycin (GenDepot, #CA005-010). All cells were incubated at 37 °C in a humidified chamber supplemented with 5% CO_2. HEK293T cells were later processed according to the needs of specific experiments (described below).

Patient-derived cell lines

Primary fibroblasts from the *PUM1* PADDAS patient and the age- and sex-matched controls were generated as previously described (1). Briefly, cells were isolated from skin biopsies taken from the patient or age-matched controls using standard methodology (Barch and Association of Cytogenetic Technology, 1991) and placed in a transport medium (Ham's F10, Thermo Scientific, #11550043). The skin specimen was later removed from the transport medium using a sterile technique (in a Class II biohazard cabinet) and transferred to a sterile Petri dish where it was cut into small pieces (< 0.5 mm) using sterile scalpel blades. These pieces were transferred to the lower surface of a 25 cm^2 culture flask (6-8 pieces per flask) which had been pre-moistened with 1-2 mL of AmnioMAX Complete Medium (Thermo Scientific, #11269016) supplemented with 1% penicillin/streptomycin (GenDepot, #CA005-010). Cell cultures were maintained at 37 °C in a humidified incubator supplemented with 5% CO_2. When cell growth was observed around the edges of the tissue, usually 3 to 5 days later, 2 to 3 mL of AmnioMAX Complete Medium were added. Once growth was established and the tissue was anchored to the flask, another 8 mL of AmnioMAX Complete Medium was added. Thereafter, the medium was renewed every 3 to 4 days until ready for sub-culturing.

Lymphoblastoid cells from *PUM1* PRCA patients and the age- and sex-matched controls were generated as previously described (1). Briefly, lymphoblastoid suspension cell cultures were grown in RPMI 1640 medium (Invitrogen, #11875093) supplemented with 10% heat-inactivated fetal bovine serum (Atlanta Biological, Flowery Branch, #S11195H) and 1% penicillin/streptomycin (GenDepot, #CA005-010). Cell cultures were maintained at 37°C in a humidified incubator supplemented with 5% CO_2. Medium was renewed every 2 to 3 days.

Immunoprecipitation (IP) experiments using mouse brain tissue

Mouse brain tissues were gathered from an equal number of 10-week-old male and female mice. For whole-brain experiments, we combined and homogenized two 10-week-old wild-type mouse brains per

sample (1 female and 1 male), aliquoting half of each sample for IP against either Pum1 or IgG, then performed six biological replicates (12 mice total) for each mass spec experiment against IP-Pum1 and IP-IgG. For experiments on the hippocampus, cerebellum, and cortex, we needed much larger numbers of mice: we combined cerebellar and cortical tissues from eight wild-type mice (4 male and 4 female) and performed the experiment in triplicate (total of 24 mice), while for hippocampus we combined tissues from ten wild-type mice (5 female and 5 male) for three experiments (a total of 30 mice).

Samples were processed with a dounce homogenizer using a lysis buffer consisting of 200mM $NaCl_2$, 100mM $NaPO_4$, 20mM Hepes pH 7.4, 1% Triton X (which should disrupt all but the strongest protein-protein interactions) and complemented by 1X of Xpert Protease and 1X of Phosphatase Inhibitor Cocktail Solutions (GenDepot, #P3100-100, #P3200-020). Following homogenization, the samples were placed on ice for 15 minutes then centrifuged at 14,800 rpm at 4°C for 25 minutes to remove the debris from the supernatant. The supernatant was then moved to 1.5 ml tubes (Beckman microfuge tube #357448) and spun down in a Beckman ultra-centrifuge (Optima Max XP) at 4°C for 25 minutes at 44,000 rpm. 10% of the protein lysate was stored as input and only 1% was loaded for western blot. The protein extract was later divided into two aliquots, one for IP against the protein of interest (antibodies listed below) and the other for IP against IgG, and was then incubated with 30 µL of Dynabeads™ Protein G (Invitrogen, #10004D) and 5 µg of antibody overnight at 4°C on a rotisserie tube rotator. The next day, the beads were washed four times with the same lysis buffer used for IP and resuspended in 40µL of elution buffer (consisting of lysis buffer, NuPAGE 10X Reducing Agent [Invitrogen, #NP0009], NuPAGE LDS sample buffer at 1X final concentration [Invitrogen, #NP0007]) and boiled at 95°C for 10 minutes before the samples were loaded in the NuPAGE 4%–12% Bis-Tris Gels (Invitrogen, #NP0335BOX & #NP0336BOX) for further resolution and western blot analysis.

For the IP with RNase treatment, the beads were resuspended in 400 µL of lysis buffer after the three final washes and divided into two separate 1.5 ml tubes of 200 µL each. To establish the dose required to remove all RNA, we tested different amounts of RNase I (Invitrogen, #EN0602) and found that 4 µL was enough to render RNA undetectable both by denaturing gel and cDNA amplification. This sample and the negative control (i.e., one without RNase treatment) were incubated at 37°C for 15 min on a rotisserie tube rotator. After incubation, all the samples were washed one last time with 500 µL of lysis buffer and then eluted in 20 µL of elution buffer. We used the same protocol for all the IP processed by mass spectrometry.

The antibodies used for IP were: goat α-PUM1 (Bethyl Laboratories, #A300-201A), rabbit α-PUM2 (Bethyl Laboratories, #A300-202A), rabbit α-FMRP (Abcam Cambridge, #ab17722), rabbit α-AGO2 (Abcam Cambridge, #ab32381), rabbit α-NeuN (Thermo Fisher Scientific, #PA5-37407), rabbit α-CNOT1 (Cell Signaling Technology, #44613), rabbit α-MOV10 (Bethyl Laboratories, #A301-571A), and

rabbit α-ANAPC1 (Bethyl Laboratories, #A301-653A).

Please note that *in vivo* IPs from brain lysates present certain challenges that are not encountered *in vitro*. Whereas the total lysate from cells is usually 200µl-300µl, the brain lysate is made in a large volume, usually 1.5 to 2.4 ml, depending on the size of the brain or brain region. This means that in a normal western blot that accommodates 30-40µl total volume, including reducing buffer and loading blue, we cannot load more than 1%-3% from the total brain lysate as input. Therefore, when we pull down a protein of interest (Pum1) and immunoblot for the same protein compared to a standard input (loading the entire IP in one gel), the resulting IP band will be much darker than the input. We then need to expose the Input from the same membrane much longer to visualize it—this is common practice when working with *in vivo* tissues (2-7).

Immunoprecipitation experiments from HEK293T and patient-derived cell lines

HEK293T cells and patient-derived fibroblasts or lymphoblastoid cells were lysed by pipetting up and down with a 1000µl tip in a lysis buffer consisting of 200mM $NaCl_2$, 100mM $NaPO_4$, 20mM Hepes pH 7.4, 1% Triton X and complemented by 1X of Xpert Protease and 1X of Phosphatase Inhibitor Cocktail (GenDepot, #P3100-100, #P3200-020). The rest of the protocol is the same as described above for mouse brain tissue, except that we used 2.5 µg of primary antibody for IP.

Co-Immunoprecipitation in-gel digestion for mass spectrometry

Immunoprecipitated samples were separated on NuPAGE 4-12% gradient SDS-PAGE (Invitrogen, #NP0335BOX & #NP0336BOX) and stained with SimplyBlue (Invitrogen, #LC6060). Protein gel slices were excised and *in-gel* digestion performed as previously described (8), with minor modifications. Gel slices were washed with 1:1 Acetonitrile and 100mM ammonium bicarbonate for 30 min then dehydrated with 100% acetonitrile for 10 min until shrunk. The excess acetonitrile was then removed and the slices dried in a speed-vacuum at room temperature for 10 minutes. Gel slices were reduced with 5 mM DTT for 30 min at 56^{o}C in an air thermostat, cooled down to room temperature, and alkylated with 11 mM IAA for 30 min with no light. Gel slices were then washed with 100 mM of ammonium bicarbonate and 100% acetonitrile for 10 min each. Excess acetonitrile was removed and dried in a speed-vacuum for 10 min at room temperature and the gel slices were re-hydrated in a solution of 25 ng/µl trypsin in 50 mM ammonium bicarbonate for 30 min on ice and digested overnight at 37 ^{o}C in an air thermostat. Digested peptides were collected and further extracted from gel slices in extraction buffer (1:2 ratio by volume of 5% formic acid: acetonitrile) at high speed, shaking in an air thermostat. The supernatants from both extractions were combined and dried in a speed-vacuum. Peptides were dissolved in 3% acetonitrile/0.1% formic acid.

Liquid chromatography with tandem mass spectrometry (LC-MS/MS)

The Thermo Scientific Orbitrap Fusion Tribrid mass spectrometer was used for peptide tandem mass spectroscopy (MS/MS). Desalted peptides were injected in an EASY-Spray^{TM} PepMap^{TM} RSLC C18 50cm X 75cm ID column (Thermo Scientific) connected to the Orbitrap Fusion^{TM} Tribrid^{TM}. Peptide elution and separation were achieved at a non-linear flow rate of 250 nl/min using a gradient of 5%-30% of buffer B (0.1% (v/v) formic acid, 100% acetonitrile) for 110 minutes, maintaining the temperature of the column at 50 °C during the entire experiment. Survey scans of peptide precursors are performed from 400 to 1500 *m/z* at 120K full width at half maximum (FWHM) resolution (at 200 *m/z*) with a 2 x 10^5 ion count target and a maximum injection time of 50 ms. The instrument was set to run in top speed mode with 3-second cycles for the survey and the MS/MS scans. After a survey scan, MS/MS was performed on the most abundant precursors, i.e., those ions that had a charge state between 2 and 6, and an intensity of at least 5000, by isolating them in the quadrupole at 1.6 Th. We used collision-induced dissociation (CID) with 35% collision energy and detected the resulting fragments with the rapid scan rate in the ion trap. The automatic gain control (AGC) target for MS/MS was set to 1 x 10^4 and the maximum injection time was limited to 35ms. The dynamic exclusion was set to 45s with a 10ppm mass tolerance around the precursor and its isotopes. Monoisotopic precursor selection was enabled.

LC-MS/MS data analysis

Raw mass spectrometric data were analyzed using the MaxQuant environment v.1.6.1.0 (9) and Andromeda for database searches (10) at default settings with a few modifications. The default was used for first search tolerance and main search tolerance (20 ppm and 6 ppm, respectively). MaxQuant was set up to search with the reference mouse proteome database downloaded from Uniprot (https://www.uniprot.org/proteomes/UP000000589). MaxQuant searched for trypsin digestion with up to 2 missed cleavages. Peptide, site and protein false discovery rates (FDR) were all set to 1% with a minimum of 1 peptide needed for identification; label-free quantitation (LFQ) was performed with a minimum ratio count of 1. The following modifications were used for protein quantification: oxidation of methionine (M), acetylation of the protein N-terminus, and deamination for asparagine or glutamine (NQ). Results obtained from MaxQuant were further analyzed using the Perseus statistical package (11) that is part of the MaxQuant distribution. Protein identifications were filtered for common contaminants. Proteins were considered for quantification only if they were found in at least two replicate groups. Significant alterations in protein abundance were determined by ANOVA with a threshold for significance of $P < 0.05$ (permutation-based FDR correction). Pum1 protein interactors were later considered if they were found in at least five out of six mass spec experiments for whole brain and in at

least two out of three experiments for each respective brain region with a fold-change of >1.5 between LFQ-PUM1-WT and LFQ-IgG-WT (see Supplemental Table 1).

Protein-protein interaction map

The protein-protein interaction map for the whole brain (Supplemental Figure 2A**)** was generated by Cytoscape (https://cytoscape.org/) (12) and interactions were inferred from Corum (13) and the Human Protein Atlas (14) by g:GOSt, which is a package of g:Profiler (https://biit.cs.ut.ee/gprofiler/gost) (15). The brain region-specific map (Figure 1A) was generated by Cytoscape.

Protein quantification and western blot analysis

Patient-derived lymphoblastoid, fibroblast cell lines, and control cell lines were collected at 6 × 10^6 cell confluence and processed for protein extraction. For mouse tissues, we processed either half of the whole brain (the other half was processed for RNA extraction, see below) or the entire hippocampus, cortex, or cerebellum for protein extraction. Mouse tissues or cell pellets were subsequently lysed with modified RIPA buffer consisting of 25 mM Tris-HCL, pH 7.6, 150 mM NaCl, 1.0% Tween 20, 1.0% sodium deoxycholate, 0.1% SDS, completed with 1X Xpert Protease and 1X Phosphatase Inhibitor Cocktail Solutions (GenDepot, #P3100-100 & #P3200-020). Cells were lysed by pipetting them up and down with a p1000 tip and then placed on ice for 20 min followed by centrifugation at 14,800 rpm at 4°C for 25 minutes. Mouse brain tissues were pipetted up and down by syringe needles—starting from an 18G 1½" (Becton Dickson, #305196), moving to 21G 1½" (Becton Dickson, #305167) and finally to a 26G 1½" (Becton Dickson, #305111) needle—until the lysate passed through the needle smoothly. Proteins were quantified by Pierce BCA Protein Assay Kit (Thermo Scientific, # PI23225) and their absorbance measured by NanoDrop OneC (Thermo Scientific). Proteins were resolved by high resolution NuPAGE 4%–12% Bis-Tris Gel (Invitrogen, #NP0335BOX & #NP0336BOX) according to the manufacturer's instructions. All the blots were acquired on the G:BOX Chemi XX9 machine (Syngene; Frederick, MD) using GeneSys software 1.6.5.0. Gel exposures were determine by the software.

Antibodies used for western blot experiments were: goat α-PUM1 [1:2500, (Bethyl Laboratories, #A300-201A)], rabbit α-PUM1 [1:2000, (Abcam Cambridge, #ab92545)], rabbit α-PUM2 [1:2000, (Bethyl Laboratories, # A300-202A)], rabbit α-FMRP [1:1000, (Abcam Cambridge, #ab17722)], rabbit α-AGO2 [1:1000, (Abcam Cambridge, #ab32381)], rabbit α-NeuN (Rbfox3) [1:1000, (Thermo Scientific, #PA5-37407)], rabbit α-CNOT1 [1:1000, (Cell Signaling Technology, #44613)], rabbit α-MOV10 [1:2000, (Bethyl Laboratories, #A301-571A)], and mouse α-GAPDH [1:10000, (Millipore, #CB1001)].

RNA extraction and quantitative real-time PCR (qPCR)

Human fibroblast, lymphoblastoid, and respective control cell lines were harvested at 6 X 10^6 confluence prior to RNA extraction. For mouse tissues, half of the whole brain (the other half was processed for protein extraction, see above) or the entire hippocampus, cortex, or cerebellum were processed for RNA extraction. The RNA was collected for both human cells, mouse brain and brain region tissues using the miRNeasy kit (QIAGEN, # 217004) according to the manufacturer's instructions. RNA was quantified using NanoDrop OneC (Thermo Fisher Scientific). cDNA was synthesized using Quantitect Reverse Transcription kit (QIAGEN, # 205313) starting from 1 µg of RNA. Quantitative RT-polymerase chain reaction (qRT-PCR) experiments were performed using the CFX96 Touch Real-Time PCR Detection System (Bio-Rad Laboratories, Hercules) with PowerUP SYBR Green Master Mix (Applied Biosystems, #A25743). Real-time PCR runs were analyzed using the comparative C_T method normalized against the housekeeping human gene *GAPDH* or mouse *Gapdh*, depending on the experiment (16).

Fibroblast patient-derived cell lines transfection

Fibroblasts from age- and sex-matched healthy controls and from a female PADDAS patient were seeded at 80% of confluency in 6-well plates (~150.000 cells/well). The day after, 500ng of pRK5-CMV-Myc-Pum1 or pRK5-CMV-Myc-Empty plasmids were transfected in antibiotic-free DMEM (GenDepot, #CM002-320) using Lipofectamine LTX with Plus Reagent (Thermo Fisher, #15338030) according to the manufacturer's protocol. After 5 hours we replaced the media with new complete DMEM supplemented with 10% of heat-inactivated fetal bovine serum (FBS [GenDepot, #F0901-050]) and 1% penicillin/streptomycin (GenDepot, #CA005-010). Cells were incubated at 37 °C in a humidified chamber supplemented with 5% CO2 and collected after 72 hours for RNA and protein extraction.

MicroRNA library construction and sequencing

Library preparation and microRNA sequencing was performed by LC Sciences according to the following criteria. Total RNA was extracted from cerebellum of WT and *Pum1*$^{-/-}$ male and female at 10 weeks of age in triplicate, for a total of 12 samples using the miRNeasy kit (QIAGEN, # 217004) according to the manufacturer's instructions. The total RNA quality and quantity were assessed with Bioanalyzer 2100 (Agilent Technologies, Santa Clara) with RIN number > 7.0. Approximately 1 µg of total RNA were used to prepare the small RNA library according to the protocol of TruSeq Small RNA Sample Prep Kits (Illumina, San Diego). Then the single-end sequencing 50bp was performed on an Illumina Hiseq 2500 at LC Sciences (Hangzhou, China) following the vendor's recommended protocol.

MicroRNA sequencing bioinformatic analysis

Raw reads were subjected to an in-house program, ACGT101-miR (LC Sciences, Houston), to remove adapter dimers, junk, common RNA families (rRNA, tRNA, snRNA, snoRNA), and repeats. Subsequently, unique sequences of 18–26 nucleotides in length were mapped to specific species precursors in miRBase 22.0 (http://www.mirbase.org/) by BLAST search to identify known miRNAs and novel 3p- and 5p-derived miRNAs. Length variation at both 3' and 5' ends and one mismatch inside of the sequence were allowed in the alignment. The unique sequences mapping to specific species of mature miRNAs in hairpin arms were identified as known miRNAs. The unique sequences mapping to the other arm of known specific species precursor hairpins opposite the annotated mature miRNA-containing arm were considered to be novel 5p- or 3p-derived miRNA candidates. The remaining sequences were mapped to other selected species precursors (with the exclusion of specific species) in miRBase 22.0 by BLAST search, and the mapped pre-miRNAs were further BLASTed against the specific species genomes to determine their genomic locations. The last two were also defined as known miRNAs. The unmapped sequences were BLASTed against the specific genomes, and the hairpin RNA structures containing sequences were predicted from the flank 80 nt sequences using RNAfold software (http://rna.tbi.univie.ac.at/cgi-bin/RNAWebSuite/RNAfold.cgi). The criteria for secondary structure prediction were: (1) number of nucleotides in one bulge in stem (≤12), (2) number of base pairs in the stem region of the predicted hairpin (≥16), (3) cutoff of free energy (kCal/mol ≤-15), (4) length of hairpin (up and down stems + terminal loop ≥50), (5) length of hairpin loop (≤20), (6) number of nucleotides in one bulge in mature region (≤8), (7) number of biased errors in one bulge in mature region (≤4), (8) number of biased bulges in mature region (≤2), (9) number of errors in mature region (≤7), (10) number of base pairs in the mature region of the predicted hairpin (≥12), (11) percent of mature region in stem (≥80).

Gene Set Enrichment Analysis (GSEA)

GSEA was performed as previously described (17). The cumulative distribution function was conducted by performing 1000 random gene-set membership assignments. A nominal p-value < 0.01 and an FDR < 0.25 were used to assess the significance of the enrichment score (ES). HITS-CLIP data, and the respective rank, were obtained from the literature and were initially acquired as follows: Pum1 and Pum2 from neonatal murine brains (18), Fmrp from cerebellum, cortex, and hippocampus together (19), Ago2 from neocortex at embryonic day 13 (20), Rbfox3 from mouse brain (age not specified) (21), Nova from mouse brain (age not specified) (22), Ptpb2 from neocortex at embryonic day 18.5 (23), Mbnl2 from hippocampus at 8-12 weeks of age (24), and Apc from mouse brain at embryonic day 14 (25).

Gene ontology analyses

Gene ontology analyses were performed with David Gene Ontology (GO). For Figure 1B, Supplemental Figure 12B and C only categories with FDR<0.05 were considered; while for Supplemental Figure 11D only categories with FDR<0.01 were considered. David GO for the Pum1 interactome in Figure 1B considered the entire interactome as background. For the GO regarding the HITS-CLIP targets shared among Pum1, Pum2, Fmrp, Ago2, and Rbfox3 (Supplemental Figure 12B and C), we considered the entire set of all targetomes together as background. Regarding the Synaptic (Syn) GO analysis, brain-expressed genes were used as background (26).

Myc and GST cloning procedure with in vitro immunoprecipitation (IP) assays

Human *PUM1* full-length cDNA was amplified by PCR and subcloned in a pRK5 plasmid containing the Myc tag sequence (Addgene, pRK5-Myc-Parkin #17612) at the N-terminal by using SalI (New England Biolabs, # R3138S) and NotI (New England Biolabs, #R0189S) restriction enzymes to replace *Parkin* with *PUM1*. For GST, the human full-length *PUM1* cDNA was, again, subcloned first in the pRK5 plasmid containing the GST tag sequence (Addgene, pRK5-HA GST RagC wt, #19304) at the N-terminal by using SalI and NotI restriction enzymes to replace *RagC* with *PUM1*. Human *FMRP*, *AGO2* and *CNOT1*, full-length cDNA were cloned and contain the GST tag sequence at the N-terminal, as described for GST-*PUM1*.

To introduce the T1035S or R1147W mutations we used the QuikChange II XL Multi Site-Directed Mutagenesis kit (Agilent Technologies, #200521). The primers for the single mutagenesis experiments were designed by QuikChange software (Stratagene, San Diego, https://www.genomics.agilent.com/primerDesignProgram.jsp).

For IP, HEK293T cells were seeded in 6-well plates for 24 h and then transfected with 250 ng of either WT or mutant PUM1 plasmid with one of the interactors using the jetPRIME Transfection Reagent (Polyplus transfection, #55-132) as per the manufacturer's protocol. pRK5-Myc empty plasmid (no cDNA) was used as a negative control. After 48 h, the cells were collected and processed for immunoprecipitation. Protein lysates were incubated overnight at 4°C with mouse α-Myc antibody (1:400, [Cell Signaling Technologies, #2276]) on a rotisserie tube rotator. The next day, the beads were washed four times with an IP lysis buffer and resuspended in 40 µL elution buffer (lysis buffer, NuPAGE 10X Reducing Agent [Invitrogen, #NP0009], NuPAGE LDS sample buffer 4X [Invitrogen, #NP0007]) and boiled at 95°C for 10 minutes before loading the samples in NuPAGE 4%–12% Bis-Tris Gels (Invitrogen, #NP0335BOX & #NP0336BOX) for further resolution and western blot analysis. Antibodies: mouse α-Myc antibody [1:2000, (Cell Signaling Technologies, #2276)], rabbit α-GST antibody [1:1000, (Cell Signaling Technologies, #2625)], mouse α-GAPDH [1:10000, (Millipore, #CB1001)].

Primers

For the qPCR analysis to unambiguously distinguish spliced cDNA from genomic DNA contamination, specific exon primers were designed to amplify across introns of the gene tested. The primers for all genes tested were designed with Primer3 (27, 28). Cloning primers were manually designed to amplify the longest spliced gene isoform tested; if there was more than one isoform according to the UCSC Genome Browser (https://genome.ucsc.edu/), we chose the longest. See Supplemental Table 7 for primer sequences.

References

1. Gennarino VA, Palmer EE, McDonell LM, Wang L, Adamski CJ, Koire A, et al. A mild PUM1 mutation is associated with adult-onset ataxia, whereas haploinsufficiency causes developmental delay and seizures. *Cell.* 2018;172(5):924-36 e11.
2. De Maio A, Yalamanchili HK, Adamski CJ, Gennarino VA, Liu Z, Qin J, et al. RBM17 Interacts with U2SURP and CHERP to Regulate Expression and Splicing of RNA-Processing Proteins. *Cell Rep.* 2018;25(3):726-36 e7.
3. Lee Y, Samaco RC, Gatchel JR, Thaller C, Orr HT, and Zoghbi HY. miR-19, miR-101 and miR-130 co-regulate ATXN1 levels to potentially modulate SCA1 pathogenesis. *Nat Neurosci.* 2008;11(10):1137-9.
4. Rousseaux MWC, Tschumperlin T, Lu HC, Lackey EP, Bondar VV, Wan YW, et al. ATXN1-CIC Complex Is the Primary Driver of Cerebellar Pathology in Spinocerebellar Ataxia Type 1 through a Gain-of-Function Mechanism. *Neuron.* 2018;97(6):1235-43 e5.
5. Di Grazia A, Marafini I, Pedini G, Di Fusco D, Laudisi F, Dinallo V, et al. The Fragile X Mental Retardation Protein Regulates RIPK1 and Colorectal Cancer Resistance to Necroptosis. *Cell Mol Gastroenterol Hepatol.* 2021;11(2):639-58.
6. Jin Z, Feng H, Liang J, Jing X, Zhao Q, Zhan L, et al. FGFR3 big up tri, open7-9 promotes tumor progression via the phosphorylation and destabilization of ten-eleven translocation-2 in human hepatocellular carcinoma. *Cell Death Dis.* 2020;11(10):903.
7. Lee EJ, Seo E, Kim JW, Nam SA, Lee JY, Jun J, et al. TAZ/Wnt-beta-catenin/c-MYC axis regulates cystogenesis in polycystic kidney disease. *Proc Natl Acad Sci U S A.* 2020;117(46):29001-12.
8. Shevchenko A, Tomas H, Havlis J, Olsen JV, and Mann M. In-gel digestion for mass spectrometric characterization of proteins and proteomes. *Nat Protoc.* 2006;1(6):2856-60.
9. Cox J, and Mann M. MaxQuant enables high peptide identification rates, individualized p.p.b.-range mass accuracies and proteome-wide protein quantification. *Nat Biotechnol.* 2008;26(12):1367-72.
10. Cox J, Neuhauser N, Michalski A, Scheltema RA, Olsen JV, and Mann M. Andromeda: a peptide search engine integrated into the MaxQuant environment. *J Proteome Res.* 2011;10(4):1794-805.
11. Tyanova S, Temu T, Sinitcyn P, Carlson A, Hein MY, Geiger T, et al. The Perseus computational platform for comprehensive analysis of (prote)omics data. *Nat Methods.* 2016;13(9):731-40.
12. Otasek D, Morris JH, Boucas J, Pico AR, and Demchak B. Cytoscape Automation: empowering workflow-based network analysis. *Genome Biol.* 2019;20(1):185.
13. Giurgiu M, Reinhard J, Brauner B, Dunger-Kaltenbach I, Fobo G, Frishman G, et al. CORUM: the comprehensive resource of mammalian protein complexes-2019. *Nucleic Acids Res.* 2019;47(D1):D559-D63.

14. Thul PJ, Akesson L, Wiking M, Mahdessian D, Geladaki A, Ait Blal H, et al. A subcellular map of the human proteome. *Science.* 2017;356(6340).
15. Raudvere U, Kolberg L, Kuzmin I, Arak T, Adler P, Peterson H, et al. g:Profiler: a web server for functional enrichment analysis and conversions of gene lists (2019 update). *Nucleic Acids Res.* 2019;47(W1):W191-W8.
16. Vandesompele J, De Preter K, Pattyn F, Poppe B, Van Roy N, De Paepe A, et al. Accurate normalization of real-time quantitative RT-PCR data by geometric averaging of multiple internal control genes. *Genome Biol.* 2002;3(7).
17. Subramanian A, Tamayo P, Mootha VK, Mukherjee S, Ebert BL, Gillette MA, et al. Gene set enrichment analysis: a knowledge-based approach for interpreting genome-wide expression profiles. *Proc Natl Acad Sci U S A.* 2005;102(43):15545-50.
18. Zhang M, Chen D, Xia J, Han W, Cui X, Neuenkirchen N, et al. Post-transcriptional regulation of mouse neurogenesis by Pumilio proteins. *Genes Dev.* 2017;31(13):1354-69.
19. Maurin T, Lebrigand K, Castagnola S, Paquet A, Jarjat M, Popa A, et al. HITS-CLIP in various brain areas reveals new targets and new modalities of RNA binding by fragile X mental retardation protein. *Nucleic Acids Res.* 2018;46(12):6344-55.
20. Chi SW, Zang JB, Mele A, and Darnell RB. Argonaute HITS-CLIP decodes microRNA-mRNA interaction maps. *Nature.* 2009;460(7254):479-86.
21. Weyn-Vanhentenryck SM, Mele A, Yan Q, Sun S, Farny N, Zhang Z, et al. HITS-CLIP and integrative modeling define the Rbfox splicing-regulatory network linked to brain development and autism. *Cell Rep.* 2014;6(6):1139-52.
22. Zhang C, Frias MA, Mele A, Ruggiu M, Eom T, Marney CB, et al. Integrative modeling defines the Nova splicing-regulatory network and its combinatorial controls. *Science.* 2010;329(5990):439-43.
23. Licatalosi DD, Yano M, Fak JJ, Mele A, Grabinski SE, Zhang C, et al. Ptbp2 represses adult-specific splicing to regulate the generation of neuronal precursors in the embryonic brain. *Genes Dev.* 2012;26(14):1626-42.
24. Charizanis K, Lee KY, Batra R, Goodwin M, Zhang C, Yuan Y, et al. Muscleblind-like 2-mediated alternative splicing in the developing brain and dysregulation in myotonic dystrophy. *Neuron.* 2012;75(3):437-50.
25. Preitner N, Quan J, Nowakowski DW, Hancock ML, Shi J, Tcherkezian J, et al. APC is an RNA-binding protein, and its interactome provides a link to neural development and microtubule assembly. *Cell.* 2014;158(2):368-82.
26. Koopmans F, van Nierop P, Andres-Alonso M, Byrnes A, Cijsouw T, Coba MP, et al. SynGO: An Evidence-Based, Expert-Curated Knowledge Base for the Synapse. *Neuron.* 2019;103(2):217-34 e4.
27. Koressaar T, and Remm M. Enhancements and modifications of primer design program Primer3. *Bioinformatics.* 2007;23(10):1289-91.
28. Untergasser A, Cutcutache I, Koressaar T, Ye J, Faircloth BC, Remm M, et al. Primer3--new capabilities and interfaces. *Nucleic Acids Res.* 2012;40(15):e115.